A concurrent irradiation-mechanics multiscale coupling model

Changqiu Ji[a], Yinan Cui[a*], Yang Li[b], Nasr Ghoniem[b]

[a]Applied Mechanics Lab., School of Aerospace Engineering, Tsinghua University, Beijing 100084, PR China
[b]Department of Mechanical and Aerospace Engineering, University of California Los Angeles, Los Angeles, CA, 90095, USA
*Corresponding author: cyn@mail.tsinghua.edu.cn

Abstract:

The vast majority of our current knowledge regarding the basic mechanisms controlling irradiation effect on mechanical properties is based almost entirely on the results of post-irradiation experiments or theoretical models. However, the concurrent effects of irradiation, mechanical stress, and thermal damage on the failure phenomena of materials and components remain largely unexplored due to its internal multiscale-multiphysics coupling nature. We present here a concurrent irradiation-mechanics multiscale coupling model. The concurrent evolutions of nanoscale irradiation defect clusters, microscale dislocation configurations, and mechanical responses are well captured based on coupling cluster dynamics, discrete dislocation dynamics, and the finite element methods using an effective time marching scheme. Model predictions of defect densities and size are in general agreement with experimental observations. Irradiation hardening is shown to take place also in samples undergoing concurrent irradiation-mechanical loading, similar to samples tested post-irradiation. However, the occurrence of plastic flow localization and dislocation channel formation is not accompanied with apparent yield drop (softening) under concurrent irradiation-mechanical loading conditions, which is different from the post-irradiation case.

Keywords: Concurrent effect, Irradiation, Mechanical loading, Dislocation, Irradiation defect

1 Introduction

Understanding the performance degradation of irradiation material is of great importance for the safety and reliability of nuclear fission or fusion power plants (Hill 2008, Zinkle and Busby 2009, Zinkle and Was 2013, Alawadi and Abdolvand 2020, Reali, Wenman et al. 2021, Tondro and Abdolvand 2021). Numerous efforts have been made with the aim of describing the evolution of irradiation-induced defects and establishing a link between defect densities and sizes and the degradation in mechanical performance (Victoria, Baluc et al. 2000, Chen, Miao et al. 2016, Cui, Po et al. 2017,

Rovelli, Dudarev et al. 2017, Chen, Liu et al. 2020, Shang, Fan et al. 2021). Several degradation phenomena in irradiated materials have been observed, such as irradiation hardening, embrittlement, creep, and volumetric swelling (Byun, Farrell et al. 2008, McMurtrey, Cui et al. 2015, Garud 2016, Xia, Zhang et al. 2019, Xiao 2019, Khiara, Onimus et al. 2021, Lin, Bhattacharya et al. 2021). However, the current understanding regarding the irradiation effects on these properties, in particular irradiation hardening and embrittlement, is based almost entirely on the results of post-irradiation experiments or theoretical models. In contrast, materials employed as structural components in fission or fusion reactors are exposed simultaneously to neutron irradiation, external stress, and high-temperature (Singh, Tähtinen et al. 2003, Singh, Edwards et al. 2004, Pakarinen, Tähtinen et al. 2013, Terentyev, Xiao et al. 2015). Several fundamental questions then arise: (1) what is the concurrent effects of neutron irradiation and mechanical loading on the deformation and failure process, and (2) are post-irradiation tests able to effectively determine the performance of in-reactor structures?

Previous efforts have led to a relatively clear physical picture of the generation and evolution of irradiation-induced defects (Fan, Kushima et al. 2011, Dunn, Capolungo et al. 2013, Cui, Po et al. 2017, Gu, Han et al. 2017, Sobie, Capolungo et al. 2017, Zhu, Wang et al. 2017, Nordlund, Zinkle et al. 2018, Kohnert and Capolungo 2019, Fan, Annadanam et al. 2020). Irradiation firstly causes collision cascades of displacement atoms, generating numerous Frenkel pairs as vacancies and self-interstitial atoms. These points defects diffuse, recombine, aggregate and dissociate in the material, leading to the production of high densities of nanoscale defect clusters. They are mainly characterized as stacking fault tetrahedra (SFT) and interstitial loops in face centered cubic (FCC) metals, and interstitial loops and nano-voids in body centered cubic (BCC) metals. These irradiation defects interact with other features of the microstructure, like dislocations and precipitates, resulting in the collective mechanical response of the material. On the one hand, these defects obstruct dislocation motion, leading to irradiation hardening. On the other hand, they may be swept away, absorbed, or destroyed by moving dislocations, causing the formation of defect-free channels (so-called dislocation channels or cleared channels) and the appearance of deformation localization (i.e. micro shear bands). Such deformation localization is widely observed in irradiated materials (Lee, Byun et al. 2001, Byun and Hashimoto 2006, Xiao 2019), and is believed to be one main origin of irradiation embrittlement (Byun and Hashimoto 2006, Xiao 2019), and significantly increases the susceptibility to stress corrosion cracking initiation (Was, Farkas et al. 2012, McMurtrey, Cui et al. 2015, Patra and McDowell 2015).

Irradiation hardening and deformation localization have been investigated extensively based on post-irradiated experimental tests (Byun and Hashimoto 2006, Byun, Farrell et al. 2008, Jiao and Was 2010) or theoretical analysis (Barton, Arsenlis et al. 2013, Cui, Po et al. 2018, Xiao, Terentyev et al. 2019, Cui, Cui et al. 2021). It is generally believed that the occurrence of deformation localization is accompanied by the

yield drop phenomena, and is mainly observed in irradiated materials at high irradiation doses (Zinkle and Singh 2006, Barton, Arsenlis et al. 2013). However, experiments show that these observations in the post-irradiated state are fundamentally different from those exposed to a dynamic irradiation environment in a fission or fusion reactor (Singh, Edwards et al. 2004). During in-reactor mechanical tests, the transition from the elastic to plastic regime occurs smoothly and without any sharp transient in the form of a yield drop. Instead, strain hardening and deformation localization may occur at the same time. The underlying mechanism of these discrepancies is still largely unexplored.

At present, there are very few experiments (Singh, Tähtinen et al. 2003, Singh, Edwards et al. 2004, Pakarinen, Tähtinen et al. 2013) focusing on concurrent irradiation and mechanical deformation. Neutron irradiation experiments at high temperatures and under external loading are expensive and time-consuming, and it's not easy to determine the deformation and irradiation coupling mechanism because of the limitations of experimental conditions. From the theoretical perspective, to the best of our knowledge, no model has ever been developed, which can disclose the underlying physical mechanism and at the same time explain the different experimental observations on deformation localization during post-irradiation tests and in-reactor tests.

During the past decades, modeling efforts have separately focused on either the evolution of irradiation-induced defects, or irradiation effects on the mechanical response (Cui, Ghoniem et al. 2021). For example, the method of cluster dynamics (CD) was developed to capture the nucleation and growth of defect clusters produced by irradiation(Kohnert, Wirth et al. 2018). On the other hand, the method of discrete dislocation dynamics (DDD) was capable of simulating the collective evolution of dislocations(Hussein and El-Awady 2016, Fan, Wang et al. 2021), and modeling the interaction mechanisms between dislocations and irradiation defects (Sobie, Capolungo et al. 2017, Li, Boleininger et al. 2019). Furthermore, continuum mechanics methods, like crystal plasticity and the finite element methods were advanced for relatively large-scale problems(Barton, Arsenlis et al. 2013, Jiao, Cheng et al. 2021, Li, Liu et al. 2021). Each of these methods alone cannot answer the fundamental questions regarding why the hardening behavior and the degree of plastic deformation localization of irradiated materials are different under post-irradiation and in-reactor experiments.

Mechanism-based theory and models of material response under simultaneous loading and irradiation are therefore urgently needed. The key problem here is that the generation and evolution of nanoscale irradiation-induced defects and microscale dislocations are strongly coupled. Irradiation defect kinetics is strongly influenced by the external loading condition, as well as the existence of dislocations. For example, atomistic simulations show that external stress influences the collision cascade process (Kirsanov, Kislitsin et al. 1991, Beeler, Asta et al. 2015). Recently, Li et al. (Li, Po et al. 2020) found that increasing the dislocation density inhibits the nucleation of interstitial loops. By coupling crystal plasticity and stochastic cluster dynamics method, it is found

that in in-situ tests, dislocation multiplication acts as a potent defect accumulation inhibitor, leading to a weak crystal orientation dependence and modest levels of defect hardening (Yu, Chatterjee et al. 2021). Therefore, in order to map the space of understanding the concurrent irradiation-mechanical deformation problem, the coupled dynamics of defect clusters and dislocations must be effectively described in the same framework. This leads to several challenges: (1) A time scale mismatch exists between defect cluster dynamics and discrete dislocation dynamics. (2) A spatial scale mismatch exists between point defects, nanoscale irradiation defect clusters, and the microscale complex dislocation network. In particular, different types of irradiation defect clusters coexist and evolve in irradiated materials. (3) With the increase of the irradiation dose, a high density of irradiation defects poses significant computational challenges.

This work aims at overcoming the challenges associated with coupling the dynamics of irradiation defects and dislocation assembles at different spatial and temporal scales. The main objective is to develop an integrated model that couples defect microstructure evolution with the concurrent evolution of the dislocation network under the influence of irradiation, temperature, and external loading. Details of the coupled models are presented in section 2, where we develop a necessary set of controlling equations for defect clusters, build effective sub-models of dislocation interaction with irradiation-induced defects, and present the coupling strategy. In section 3, verification cases are given to illustrate the effectiveness of the model by applying it to α-iron. Section 4 is dedicated to discussing the differences between post-irradiation and in-reactor response, while conclusions are given in section 5.

2 Model description

2.1 Basic framework

The concurrent model consists of three parts: cluster dynamics (CD), discrete dislocation dynamics (DDD), and the finite element method (FEM). The framework of the model is schematically shown in Fig. 1. The irradiation field is simulated with CD to obtain the evolution of irradiation defects as a function of the irradiation dose and temperature. The behavior of dislocations is calculated by DDD, in which the resistance effect of irradiation defects on dislocations is considered. To overcome the challenges of the huge computational cost associated with high dose irradiation, defects are coarse-grained and represented as continuous fields in the finite element method. Irradiation-induced defects are characterized using the spatial and temporal evolution of their density and mean size. In this section, each part of the integrated model will be introduced separately, and then, the parameter-passing framework and the spatio-temporal coupling strategy between each part will be presented. Although the chosen material here is α-iron, the model can be readily extended to other materials.

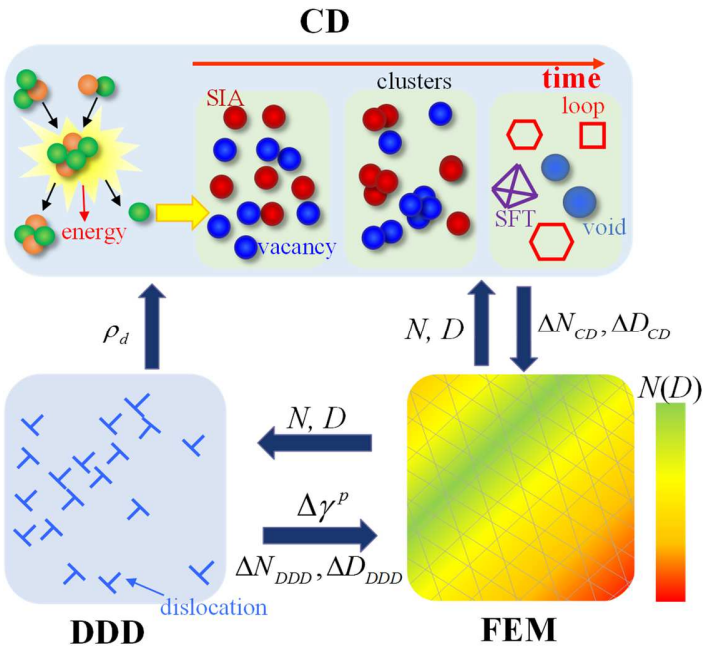

Fig. 1 Schematic of the framework and parameter passing of the model including three parts, namely clusters dynamics (CD), discrete dislocation dynamics (DDD) and the finite element method (FEM). ρ_d is the density of dislocation line, and $\Delta\gamma^p$ is the local plastic strain increment. N and D are the density and average diameter of irradiation defects, respectively. ΔN_{CD}, ΔD_{CD}, ΔN_{DDD} and ΔD_{DDD} are the increment of density and diameter of irradiation defect gained from CD and DDD, respectively.

2.2 Irradiation defect kinetics based on cluster dynamics

In this model, CD is used to calculate the nucleation and growth of irradiation-induced defects. CD modeling is a mean-field approach based on rate theory. Till now, CD remains an irreplaceable method for predicting the long-term evolution of materials under high-dose irradiation on reactor timescales(Barbu and Clouet 2007, Meslin, Barbu et al. 2008). In CD, the system is described as a population of clusters defined by the distribution functions of their size (or equivalently, the number of monomers they contain) (Mamivand, Wells et al. 2019).

Assuming that a material sample receives a uniform irradiation flux, the defect production rate is homogeneous in space and in time (Wang, Ding et al. 2018). The collision cascade is supposed to primarily lead to the generation of single point defects, vacancy clusters with 2-4 vacancies, SIA clusters with 2-3 atoms, and large immobile vacancy clusters. The considered irradiation defects and their properties in the model are listed in Table 1 and described as follows.

- Single point defects: single self-interstitial atoms (SIA) and single vacancies are spherical and migrate in 3D (Dunn and Capolungo 2015, Wang, Ding et al. 2018). They can form clusters or interact with other defects.
- Small vacancy clusters with 2~4 vacancies: di-vacancies, tri-vacancies, and tetra-vacancies are treated as spherical clusters that are mobile and migrate in 3D (Dunn and Capolungo 2015, Dunn, Muntifering et al. 2016). They can annihilate with self-interstitial atoms, absorb or dissociate single vacancies.
- Small self-interstitial clusters with 2~3 SIA: di-interstitials and tri-interstitials are two-dimensional and have similar ground-state configurations called dumbbells (Fu, Torre et al. 2004). They migrate in a quasi-1D form (Trinkaus, Singh et al. 2000, Soneda and De La Rubia 2001). Here, we simply treat them as 1D migrating loops (Dunn, Capolungo et al. 2013).
- Larger vacancy clusters: large vacancy clusters consist of ½<111> vacancy loops, <100> vacancy loops and voids. Experiments and simulations show that vacancy loops only appear in some exceptional cases (Gilbert, Yao et al. 2009, Balbuena, Aliaga et al. 2019). Spherical voids represent the lowest energy configurations for vacancy clusters of any size in Fe rather than vacancy loops (Gilbert, Yao et al. 2009). We will, therefore, ignore the vacancy loop population in CD. Vacancy clusters containing more than four vacancies are all considered spherical and immobile voids in our simulation (Fu, Torre et al. 2004, Meslin, Barbu et al. 2008, Kohnert and Wirth 2015, Dunn, Muntifering et al. 2016). They can absorb point defects and interact with all migratory species.
- Larger self-interstitial clusters: self-interstitial clusters containing more than 3 SIA are considered circular and immobile (Fu, Torre et al. 2004, Meslin, Barbu et al. 2008, Dunn and Capolungo 2015), and they can absorb other defects similar to large vacancy clusters. Although some interstitial clusters such as ½<111> and <100> interstitial loops are physically mobile (Dunn and Capolungo 2015), it is reasonable to treat all of them as immobile defects (Fu, Torre et al. 2004).

Table 1 Shape and mobility of irradiation defect clusters, I_n means self-interstitial clusters with nSIAs, and V_n means vacancy clusters with n vacancies.

Defects	I_1	I_2	I_3	$I_{>=4}$	V_1	V_2	V_3	V_4	$V_{>=5}$
Shape	sphere	loop	loop	loop	sphere	sphere	sphere	sphere	sphere
Mobility	3D	1D	1D	immobile	3D	3D	3D	3D	immobile

The concentrations of mobile defects depend on the production from cascades, reaction with other clusters, thermal dissociation and sink absorption. Based on the shape and mobility features of defects, the kinetic mass conservation equations of defect concentrations are as follows,

$$\frac{dC_v}{dt}=\frac{G^{NRT}}{\Omega}\eta(1-\varepsilon_{2v}-\varepsilon_{3v}-\varepsilon_{4v}-\left(1-V_{cap}N_{vo}\right)\varepsilon_{nv})+\beta_{2v}^{i}C_iC_{2v}+\beta_{3v}^{2i}C_{2i}C_{3v}$$
$$+\beta_{4v}^{3i}C_{3i}C_{4v}+2\alpha_{2v}^{v}C_{2v}+\alpha_{3v}^{v}C_{3v}+\alpha_{4v}^{v}C_{4v}-R_{iv}C_vC_i-\beta_{2i}^{v}C_vC_{2i}-\beta_{3i}^{v}C_vC_{3i} \quad (1)$$
$$-\beta_{v}^{v}C_vC_v-\beta_{2v}^{v}C_vC_{2v}-\beta_{3v}^{v}C_vC_{3v}-\beta_{4v}^{v}C_vC_{4v}-k_v^2D_vC_v$$

$$\frac{dC_{2v}}{dt}=\frac{G^{NRT}}{\Omega}\frac{\eta\varepsilon_{2v}}{2}+\frac{1}{2}\beta_{v}^{v}C_vC_v+\beta_{3v}^{i}C_iC_{3v}+\beta_{4v}^{2i}C_{2i}C_{4v}+\alpha_{3v}^{v}C_{3v}-\alpha_{2v}^{v}C_{2v}$$
$$-\beta_{2v}^{i}C_iC_{2v}-\beta_{2v}^{2i}C_{2i}C_{2v}-\beta_{3i}^{2v}C_{3i}C_{2v} \quad (2)$$
$$-\beta_{2v}^{v}C_vC_{2v}-\beta_{2v}^{2v}C_{2v}C_{2v}-\beta_{3v}^{2v}C_{3v}C_{2v}-\beta_{4v}^{2v}C_{4v}C_{2v}-k_{2v}^2D_{2v}C_{2v}$$

$$\frac{dC_{3v}}{dt}=\frac{G^{NRT}}{\Omega}\frac{\eta\varepsilon_{3v}}{3}+\beta_{2v}^{v}C_vC_{2v}+\beta_{4v}^{i}C_{4v}C_i+\alpha_{4v}^{v}C_{4v}-\alpha_{3v}^{v}C_{3v}$$
$$-\beta_{3v}^{i}C_iC_{3v}-\beta_{3v}^{2i}C_{2i}C_{3v}-\beta_{3v}^{3i}C_{3i}C_{3v} \quad (3)$$
$$-\beta_{3v}^{v}C_vC_{3v}-\beta_{3v}^{2v}C_{2v}C_{3v}-\beta_{3v}^{3v}C_{3v}C_{3v}-\beta_{4v}^{3v}C_{4v}C_{3v}-k_{3v}^2D_{3v}C_{3v}$$

$$\frac{dC_{4v}}{dt}=\frac{G^{NRT}}{\Omega}\frac{\eta\varepsilon_{4v}}{4}+\beta_{3v}^{v}C_vC_{3v}+\frac{1}{2}\beta_{2v}^{2v}C_{2v}C_{2v}-\alpha_{4v}^{v}C_{4v}$$
$$-\beta_{4v}^{i}C_iC_{4v}-\beta_{4v}^{2i}C_{2i}C_{4v}-\beta_{4v}^{3i}C_{3i}C_{4v} \quad (4)$$
$$-\beta_{4v}^{v}C_vC_{4v}-\beta_{4v}^{2v}C_{2v}C_{4v}-\beta_{4v}^{3v}C_{3v}C_{4v}-\beta_{4v}^{4v}C_{4v}C_{4v}-k_{4v}^2D_{4v}C_{4v}$$

$$\frac{dC_i}{dt}=\frac{G^{NRT}}{\Omega}\eta(1-\varepsilon_{2i}-\varepsilon_{3i})+\beta_{2i}^{v}C_vC_{2i}+\beta_{3i}^{2v}C_{2v}C_{3i}+2\alpha_{2i}^{i}C_{2i}+\alpha_{3i}^{i}C_{3i}$$
$$-\beta_{i}^{i}C_iC_i-\beta_{2i}^{i}C_iC_{2i}-\beta_{3i}^{i}C_iC_{3i} \quad (5)$$
$$-R_{iv}C_vC_i-\beta_{2v}^{i}C_iC_{2v}-\beta_{3v}^{i}C_iC_{3v}-\beta_{4v}^{i}C_iC_{4v}-k_i^2D_iC_i$$

$$\frac{dC_{2i}}{dt}=\frac{G^{NRT}}{\Omega}\frac{\eta\varepsilon_{2i}}{2}+\frac{1}{2}\beta_{i}^{i}C_iC_i+\beta_{3i}^{v}C_vC_{3i}+\alpha_{3i}^{i}C_{3i}-\alpha_{2i}^{i}C_{2i}$$
$$-\beta_{2i}^{i}C_iC_{2i}-\beta_{2i}^{2i}C_{2i}C_{2i}-\beta_{3i}^{2i}C_{3i}C_{2i} \quad (6)$$
$$-\beta_{2i}^{v}C_vC_{2i}-\beta_{2i}^{2v}C_{2v}C_{2i}-\beta_{3v}^{2i}C_{3v}C_{2i}-\beta_{4v}^{2i}C_{4v}C_{2i}-k_{2i}^2D_{2i}C_{2i}$$

$$\frac{dC_{3i}}{dt}=\frac{G^{NRT}}{\Omega}\frac{\eta\varepsilon_{3i}}{3}+\beta_{2i}^{i}C_iC_{2i}-\alpha_{3i}^{i}C_{3i}-\beta_{3i}^{i}C_iC_{3i}-\beta_{3i}^{2i}C_{2i}C_{3i}-\beta_{3i}^{3i}C_{3i}C_{3i} \quad (7)$$
$$-\beta_{3i}^{v}C_vC_{3i}-\beta_{3i}^{2v}C_{2v}C_{3i}-\beta_{3i}^{3v}C_{3v}C_{3i}-\beta_{4v}^{3i}C_{4v}C_{3i}-k_{3i}^2D_{3i}C_{3i}$$

where the subscripts *v*, *2v*, *3v*, *4v*, *i*, *2i* and *3i* denote single vacancies, di-vacancies, tri-vacancies, tetra-vacancies, single SIA, di-interstitials and tri-interstitials, respectively. ε_{2v} is the fraction of vacancies produced in the form of di-vacancies, and parameters such as ε_{3v}, ε_{4v}, ε_{2i} and ε_{3i} have similar meanings. G^{NRT} is the standard dose rate and Ω is the atomic volume of iron. η is cascade efficiency, which means the ratio between the number of the point defect monomers at the end of the cascade stage to the total number of these defects created at the initial cascade stage.

Determination of the cluster reaction rates, including defect annihilation, clustering, dissociation and trapping at sinks, is of prime importance in the CD model. The recombination rate of single SIA and single vacancy is given as $R_{iv} = 4\pi r_{iv}\left(D_i + D_v\right)$ (Pokor, Brechet et al. 2004, Chen, Wei et al. 2019), where r_{iv} is recombination radius. D_k is the diffusion coefficient of *k*-type monomers and is expressed as $D_k = D_{0,k}\exp\left(-\frac{E_k^m}{k_B T}\right)$ (Dunn, Agudo-Merida et al. 2014, Kohnert and Wirth 2015, Kohnert, Wirth et al. 2018), where $D_{0,k}$ is diffusion pre-exponential factor and E_k^m is the migration energy for the *k*-type cluster (*k=v, 2v, 3v, 4v, i, 2i, 3i).* k_B is the Boltzmann constant and *T* is temperature in Kelvin. The fidelity of the cluster diffusivity parameters is of paramount importance to the success of these models (Kohnert and Wirth 2015).

In the CD equations for species concentrations, α means emission rate and β means reaction rate, which demonstrate the stability and mobility of defect clusters in the material. The emission rate is written as $\alpha_{ni}^{i} = \beta_{(n-1)i}^{i}\exp\left(-\frac{E_{ni}^B}{k_B T}\right)$ and $\alpha_{nv}^{v} = \beta_{(n-1)v}^{v}\exp\left(-\frac{E_{nv}^B}{k_B T}\right)$ for SIAs and vacancies (Gokhman and Bergner 2010, Kohnert and Wirth 2015), where E_{ni}^B and E_{nv}^B are binding energy of small clusters with size *n*. β depends on the shape and motion way of the two interacting clusters. The expression of reaction rate and sink strength are summarized in Fig. 2.

For the case of 3D migrating spherical defects *P* interacting with 3D migrating spherical defects *Q*, $\beta_P^Q = 4\pi(r_P + r_Q)(D_P + D_Q)$. It is the sum of the reaction rate of a 3D diffusing cluster *P* combining with an immobile defect *Q* and the reaction rate of an immobile defect *P* combining with a 3D diffusing cluster *Q* (Marian and Bulatov 2011, Dunn and Capolungo 2015, Kohnert and Wirth 2015, Kohnert, Wirth et al. 2018, Chen, Wei et al. 2019). Here, the subscripts *P, Q=v,2v,3v,4v,i*, representing the type of small clusters. The point defects and small clusters are described as spherical having radii $r = \left(\frac{3\Omega n}{4\pi}\right)^{\frac{1}{3}}$, while the radii of small planar clusters are written as $r = \left(\frac{n\Omega}{\pi b}\right)^{\frac{1}{2}}$ (Dunn,

Capolungo et al. 2013, Kohnert, Wirth et al. 2018). Here, n is the size of clusters, and b is the Burgers vector magnitude of iron.

For the case of 1D migrating small SIA clusters P interacting with 3D migrating spherical defects Q, their agglomeration rates are given as $\beta_P^Q = 2\pi\left(r_P + r_Q\right)D_Q + \left(\pi(r_P + r_Q)^2\right)^2 D_P C_Q$ (Golubov, Barashev et al. 2012, Dunn, Capolungo et al. 2013, Li, Po et al. 2020), here P=*2i,3i* and Q=*v,2v,3v,4v,i*. The first term represents a 3D diffusing defect reacting with an immobile planar cluster. It is worth noticing that for the reaction rate between a 3D migrating defect and an immobile defect, different shapes of the immobile clusters lead to various coefficients of expressions (Gokhman and Bergner 2010, Dunn, Capolungo et al. 2013, Chen, Wei et al. 2019). The second term represents an immobile defect reacting with a 1D diffusing small cluster. Note that the second-order reaction kinetics describes 3D migrating defects. The 1D migrating SIA clusters are represented by third-order reaction kinetics (Golubov, Barashev et al. 2012, Golubov, Barashev et al. 2015).

For the case of 1D migrating small SIA clusters P interacting with 1D migrating SIA clusters Q, their reaction rates are given as $\beta_P^Q = \left(\pi(r_P + r_Q)^2\right)^2 \left(D_P C_Q + D_Q C_P\right)$ (Dunn, Capolungo et al. 2013). Here, P, Q =*2i*, *3i*.

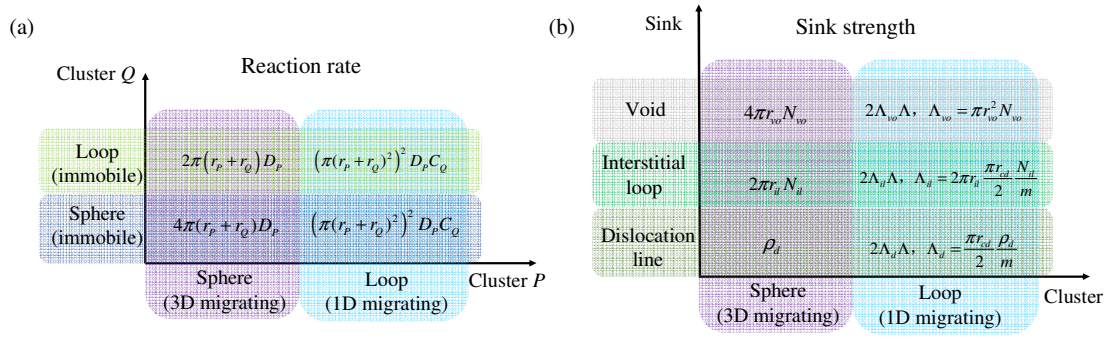

Fig. 2 (a) Reaction rate between a mobile cluster P and an immobile cluster Q. (b) Partial sink strength of immobile sinks on clusters. For k= *v*, *2v*, *3v*, *4v*, *i*, *2i* and *3i*. r_k, D_k and C_k are radius, diffusion parameter, concentration of cluster k, respectively. For k=*il* and *vo*, r_k, N_k are radius and density of defect k. ρ_d is dislocation density. Total sink strength is the sum of different partial sink strengths as $\Lambda=\Lambda_d+\Lambda_{il}+\Lambda_{vo}$. The subscripts *d*, *il* and *vo* stand for dislocation line, interstitial loop and void, respectively.

The loss rate of clusters to different types of microstructure features (sinks) is called sink strength, as shown in Fig. 2 (b). The sink strength k^2 has the units of $1/m^2$ and represents the inverse of the square of the mean free path traveled by the cluster before it is absorbed by a stationary sink (Dunn, Capolungo et al. 2013). The sink strength of vacancy clusters that migrate in 3D is (Trinkaus, Singh et al. 2000, Golubov, Barashev et al. 2012, Dunn, Capolungo et al. 2013)

$$k_j^2 = \rho_d Z_d^v + 2\pi r_{il} N_{il} Z_{il}^v + 4\pi r_{vo} N_{vo},\ j = v,\ 2v,\ 3v\ and\ 4v \tag{8}$$

where ρ_d represents the density of dislocation lines. r_{il} , r_{vo} , N_{il} and N_{vo} are the radius of interstitial loops, the radius of voids, the number density of interstitial loops and the number density of voids, respectively. The superscript *j* (*j=v, 2v, 3v* and *4v*) represents the type of small clusters, and they can be absorbed by dislocation lines, interstitial loops or voids. A dislocation bias *Z* is introduced here because dislocations preferentially absorb interstitials over vacancies, leaving more vacancies left in the sample (Gokhman and Bergner 2010, Dunn and Capolungo 2015). Similarly, for SIAs, $k_i^2 = \rho_d Z_d^i + 2\pi r_{il} N_{il} Z_{il}^i + 4\pi r_{vo} N_{vo}$. Only single crystals are considered in our model, so the sink strength of grain boundaries is ignored.

For interstitial defects migrating in 1D, the sink strength is given as (Golubov, Barashev et al. 2012, Golubov, Barashev et al. 2015, Kohnert and Wirth 2015)

$$k_j^2 = 2\left(\frac{\pi r_{cd}}{2} \left(\frac{\rho_d}{m} + 2\pi r_{il} \frac{N_{il}}{m} \right) + \pi r_{vo}^2 N_{vo} \right)^2,\ j = 2i,\ 3i\,, \tag{9}$$

where r_{cd} is the capture radius and *j=2i, 3i*. The denominator *m* comes from that because of the one-dimensional motion of the clusters, only a portion of dislocations can absorb them. Through the analysis in Appendix A, the value of *m* is set to 4.

In what follows, the nucleation and growth of sessile loops and voids will be considered. The nucleation of interstitial loops is controlled by diffusion process, while for voids, nucleation is dominated by diffusion as well as collision. Assuming that SIA clusters with a size of four interstitials and above, as well as vacancy clusters with five vacancies and above are sessile at a long-time scale (Fu, Torre et al. 2004), the nucleation rate equations for interstitial loops and voids are written as:

$$\frac{dN_{il}}{dt} = \beta_{3i}^i C_i C_{3i} + \frac{1}{2}\beta_{2i}^{2i} C_{2i} C_{2i} + \beta_{3i}^{2i} C_{2i} C_{3i} + \frac{1}{2}\beta_{3i}^{3i} C_{3i} C_{3i} \tag{10}$$

$$\begin{aligned} \frac{dN_{vo}}{dt} &= \beta_{4v}^v C_v C_{4v} + \beta_{4v}^{2v} C_{2v} C_{4v} + \beta_{4v}^{3v} C_{3v} C_{4v} + \beta_{3v}^{2v} C_{2v} C_{3v} \\ &+ \frac{1}{2}\beta_{3v}^{3v} C_{3v} C_{3v} + \frac{1}{2}\beta_{4v}^{4v} C_{4v} C_{4v} + \frac{G^{NRT} \eta \varepsilon_{nv} \left(1 - V_{cap} N_{vo}\right)}{\Omega n_v} \end{aligned} \tag{11}$$

The last term and other terms of Eq. (11) represent the contributions of collisions and diffusion to the void nucleation, respectively. ε_{nv} is the fraction of vacancies produced in the form of vacancy clusters with a size greater than four vacancies (immobile) directly, n_v is the average number of vacancies in those clusters and V_{cap} is the reciprocal of the maximum void density (Li, Po et al. 2020).

For cluster growth, the total number of defect atoms in interstitial loops and voids are expressed using S_i and S_v, respectively. Then, the evolution of S_i and S_v based on the defect concentrations are obtained (Ghoniem 1989, Ghoniem, Alhajji et al. 1992, Li, Po et al. 2020):

$$\frac{dS_i}{dt} = \Omega \begin{bmatrix} 2\pi r_{il} N_{il} (D_i C_i Z_{il}^i - D_v C_v Z_{il}^v - 2D_{2v} C_{2v} Z_{il}^v - 3D_{3v} C_{3v} Z_{il}^v - 4D_{4v} C_{4v} Z_{il}^v) \\ +2k_{il}^2 D_{2i} C_{2i} + 3k_{il}^2 D_{3i} C_{3i} \end{bmatrix} \quad (12)$$

$$\frac{dS_v}{dt} = \Omega \begin{bmatrix} 4\pi r_{vo} N_{vo} (D_v C_v + 2D_{2v} C_{2v} + 3D_{3v} C_{3v} + 4D_{4v} C_{4v} - D_i C_i) \\ -2k_{vo}^2 D_{2i} C_{2i} - 3k_{vo}^2 D_{3i} C_{3i} \end{bmatrix} \quad (13)$$

Terms in the formula represent the contribution of sessile clusters absorbing different small mobile clusters. k_{il}^2 and k_{vo}^2 are partial sink strength for 1D migrating defects (*2i*, *3i*) absorbed by interstitial loops and voids respectively, namely (Trinkaus, Singh et al. 2000, Golubov, Barashev et al. 2012)

$$k_{il}^2 = 2 \times \frac{\pi r_{cd}}{2} \times 2\pi r_{il} \frac{N_{il}}{4} \left(\frac{\pi r_{cd}}{2} \left(\frac{\rho_d}{4} + 2\pi r_{il} \frac{N_{il}}{4} \right) + \pi r_{vo}^2 N_{vo} \right) \quad (14)$$

$$k_{vo}^2 = 2 \times \pi r_{vo}^2 N_{vo} \left(\frac{\pi r_{cd}}{2} \left(\frac{\rho_d}{4} + 2\pi r_{il} \frac{N_{il}}{4} \right) + \pi r_{vo}^2 N_{vo} \right) \quad (15)$$

Then using the mean-size approximation, the average radii of the sessile loops and voids can be expressed as:

$$\left\langle \left(r_{il} \right)^2 \right\rangle \approx \left\langle r_{il} \right\rangle^2 = \frac{S_i}{\pi b N_{il}} \quad (16)$$

$$\left\langle \left(r_{vo} \right)^3 \right\rangle \approx \left\langle r_{vo} \right\rangle^3 = \frac{3S_v}{4\pi N_{vo}} \quad (17)$$

Finally, according to the chain rule, the evolution of average radii are expressed as

$$\frac{dr_{il}}{dt} = \frac{1}{2} \left(\frac{1}{\pi b N_{il} S_i} \right)^{\frac{1}{2}} \frac{dS_i}{dt} - \frac{1}{2N_{il}} \left(\frac{S_i}{\pi b N_{il}} \right)^{\frac{1}{2}} \frac{dN_{il}}{dt} \quad (18)$$

$$\frac{dr_{vo}}{dt} = \frac{1}{3} \left(\frac{3}{4\pi N_{vo} S_v^2} \right)^{\frac{1}{3}} \frac{dS_v}{dt} - \frac{1}{3} \left(\frac{3S_v}{4\pi N_{vo}^4} \right)^{\frac{1}{3}} \frac{dN_{vo}}{dt} \quad (19)$$

Till now, a CD model consisting of a set of coupled ordinary differential equations that track the evolution of all mobile monomer species and immobile clusters has been built.

2.3 Discrete dislocation dynamics

Computer simulations of discrete dislocation dynamics have now reached a relatively mature stage. The interactions of dislocations, for example, dislocation junction formation, their multiplication and annihilations can be well captured, and their influence on the mechanical behavior, such as Taylor hardening, can also be well reproduced (Zhu, Xiang et al. 2016, Akhondzadeh, Sills et al. 2020, Lu, Kan et al. 2022). Many results of these simulations have compared well with experimental data. The 3D DDD method employed here is the MoDELib (Mechanics Of Defect Evolution Library) computer code (Po, Mohamed et al. 2014). More details of the method can also be seen in our previous work (Ghoniem, Tong et al. 2000, Po, Lazar et al. 2014, Cui, Po et al. 2018). In this approach, curved dislocation lines are discretized into a succession of parametrized segments. Configurational Peach-Koehler (PK) forces are computed, and a system of equations for the motion of nodes connecting these segments is solved in a way similar to the traditional FEM (Po, Mohamed et al. 2014). The velocity of small dislocation line segments in BCC crystals is expressed by an atomistically informed mobility law (Po, Cui et al. 2016). Boundary conditions and image forces are imposed by coupling the infinite elastic field solution of dislocations to an elasticity problem in finite domains with the FEM, based on the superposition principle (Po, Mohamed et al. 2014).

Recent work has demonstrated that DDD is an effective tool to study irradiation effects (De la Rubia, Zbib et al. 2000, Arsenlis, Rhee et al. 2012, Aubry, Rhee et al. 2016, Geslin, Gatti et al. 2017, Sobie, Capolungo et al. 2017, Li, Robertson et al. 2018, Liu, Cocks et al. 2020, Osetsky and Rodney 2020). DDD can capture the interaction mechanism between dislocations and irradiation defects, get the collective interaction of dislocations, and obtain the macroscopic mechanical response of irradiated materials. We have demonstrated that the DDD method reproduces fundamental atomistic interaction mechanisms between dislocations and irradiation defects (Cui, Po et al. 2017). In our recent research, it has been used to study irradiation effects on strain bursts (Cui, Po et al. 2017) and on plastic flow localization (Po and Ghoniem 2013, Cui, Po et al. 2018, Cui, Po et al. 2018, Cui, Po et al. 2018).

2.4 Irradiation field based on the finite element method

Direct numerical simulations of the interaction between discrete dislocations and the high density of nano-sized irradiation defects in representative material volumes is computationally prohibitive at the present time (Terentyev, Monnet et al. 2013). To solve

this issue, we proposed that these high-density barriers can be described at a coarse scale through a continuous field, to obtain higher computation efficiency and capability (Cui, Po et al. 2018). To this end, the behavior for materials with super high-density defects and large external size can be understood with acceptable computation cost. Therefore, dislocation evolutions are described by discrete dislocation segments, whereas irradiation defects are coarsened as temporal and spatial dependent continuous fields.

The interaction of irradiation defects with dislocations is mainly reflected in two aspects: the hardening caused by dislocation motion hindered by defects, and the damage and destruction of irradiation defects caused by dislocation movement. Continuum equations can be developed to describe the evolution of these two variables as functions of the degree of plastic deformation. If coupling with CD and DDD is to be attempted, then one would like to describe the hardening effect of such barriers and the precise details of defect-dislocation interaction kinetics in concurrent irradiation and loading conditions.

2.4.1 Irradiation hardening model

2.4.1.1 Interstitial loops

The hardening effect induced by interstitial loops can be well described through the dispersed barrier hardening (DBH) model (Seeger 1958, Bergner, Pareige et al. 2014, Cui, Po et al. 2018)

$$\tau_{il} = \alpha_{DBH}\mu b\sqrt{N_{il}D_{il}} \tag{20}$$

where τ_{il} represents the resolved shear stress necessary to unlock a dislocation from interstitial loops with number density N_{il} and average diameter D_{il}. μ is the shear modulus and b is the Burgers vector magnitude. α_{DBH} is a dimensionless coefficient reflecting defect barrio strength. α_{DBH} is set to 0.25 according to previous work(Garner, Hamilton et al. 1981, Liu and Biner 2008, Terentyev, Grammatikopoulos et al. 2008, Bergner, Pareige et al. 2014).

2.4.1.2 Voids

Bacon–Kocks–Scattergood (BKS) model(Bacon, Kocks et al. 1973) is widely used to describe the hardening effect induced by voids, and is expressed as

$$\tau_{vo0} = \frac{\mu b}{2\pi L_{vo}}\left[\ln\left(\frac{L_{vo}}{b}\right)\right]^{\frac{1}{2}}\left[\ln\left(\frac{D_{vo}^{'}}{b}\right)+C\right]^{\frac{3}{2}} \tag{21}$$

where τ_{vo0} represents the resolved shear stress necessary to unlock a dislocation from voids with number density N_{vo} and average diameter D_{vo}. $L_{vo} = 1/\sqrt{N_{vo}D_{vo}}$ is the

average spacing of voids and $D_{vo}^{'} = D_{vo}L_{vo}/\left(D_{vo}+L_{vo}\right)$. C is a constant equal to 0.7 (Sobie, Bertin et al. 2015, Dunn, Dingreville et al. 2016). Molecular dynamics simulations show that the critical resolved shear stress to pass through voids decreases with the increase of temperature (Bacon and Osetsky 2005, Osetsky and Bacon 2005, Terentyev, Bacon et al. 2008, Osetsky and Bacon 2010). In order to reproduce the temperature effect, we proposed a temperature-dependent void hardening model based on the analysis of MD results (Bacon and Osetsky 2005, Osetsky and Bacon 2010)

$$\tau_{vo} = \tau_{vo0} - \tau_{vo0}\exp\left(-\frac{E_t}{kT}\right) \tag{22}$$

This equation considers that dislocations can overcome voids with the help of thermal activation process. A thermal activation energy E_t is introduced and determined as 0.03 eV by fitting MD data, as shown in Fig. 3.

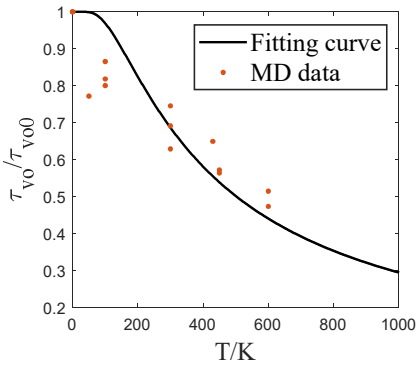

Fig. 3 Normalized value of the critical shear stress τ_{vo} induced by voids as a function of temperature T, τ_{vo0} is the critical shear stress at 0 K. MD data comes from ref (Bacon and Osetsky 2005, Osetsky and Bacon 2010).

2.4.1.3 Overall hardening

The overall hardening induced by different kinds of irradiation defects is considered based on the superposition method (Sobie, Bertin et al. 2015, Dunn, Dingreville et al. 2016)

$$\tau_{irra}^{n} = \tau_{il}^{n} + \tau_{vo}^{n}, \quad n = 2.22\,. \tag{23}$$

Under irradiation, the stress field felt by the dislocation is expressed as $\boldsymbol{\sigma} = \boldsymbol{\sigma}_0 + \boldsymbol{\sigma}_{irra}$, where $\boldsymbol{\sigma}_0$ is the stress field induced by mechanical boundary condition, image force and other dislocations.

The resistance stress field $\boldsymbol{\sigma}_{irra}$ induced by irradiation defects is

$$\boldsymbol{\sigma}_{irra}=\begin{cases}-\tau_{irra}\left(\mathbf{b}_s\otimes\mathbf{n}+\mathbf{n}\otimes\mathbf{b}_s\right)sign(\tau_{glide}),\left|\tau_{glide}\right|>\tau_{irra}\\-\tau_{glide}\left(\mathbf{b}_s\otimes\mathbf{n}+\mathbf{n}\otimes\mathbf{b}_s\right),\left|\tau_{glide}\right|\le\tau_{irra}\end{cases} \tag{24}$$

where $\mathbf{b}_s$ and $\mathbf{n}$ are the unit vectors of the Burgers vector and slip plane normal vector of the dislocation segment, respectively. $\otimes$ represents tensor product. τ_{glide} is proportional to PK force in the absence of irradiation defects. The physical meaning of the first situation $\left|\tau_{glide}\right|>\tau_{irra}$ in Eq. (24) is that the barrier stress τ_{irra} induced by the irradiation defects is lower than the driving stress induced by other stress components $\boldsymbol{\sigma}_0$. In this case, the resolved shear stress is $\tau_{glide}-\tau_{irra}sign(\tau_{glide})$. When $\left|\tau_{glide}\right|\le\tau_{irra}$, the barrier stress induced by the irradiation defects is higher than the driving stress induced by other stress components $\boldsymbol{\sigma}_0$. In this case, the dislocation cannot move. To avoid the dislocation motion along the opposite direction, the irradiation stress is set to be consistent with the magnitude of glide stress, so that the total resolved shear stress that drives the motion of dislocation is 0. The tensor expression of the resistant stress is capable of considering not only the impede effects on dislocation motion, but also its effect on the occurrence of cross slip.

2.4.2 Kinetic model of irradiation defect interaction with dislocations

After the hardening model is established, attention is placed on the damage or destruction of irradiation defects induced by dislocation motion.

2.4.2.1 Kinetic model of interstitial loops

For irradiation loops, a wide range of computer simulations show that irradiation defect clusters are either absorbed, reacted or swept away by gliding dislocations within a prescribed capture distance *y/2* (Ghoniem, Tong et al. 2001, Osetsky, Stoller et al. 2005, Cui, Po et al. 2018). As shown in Fig. 4 , consider a specific control volume *V* through which a dislocation glides and interacts with defects. If the slip area increment of the dislocation is *ΔA*, namely the area enclosed by points A, B, C and D, then the number of defects interacting with the dislocation is $y\Delta AN_{il}$. Assuming that the defect annihilation fraction is *λ*, the change in the average irradiation defect density during the interaction duration *Δt* in *V* can be expressed as,

$$\Delta N_{il}^{DDD}=-\lambda N_{il}\frac{y\Delta A}{V}=-\lambda N_{il}\frac{y\Delta\gamma^p}{b} \tag{25}$$

where ΔN_{il}^{DDD} is the reduction of defect density due to plastic deformation during the interval *Δt* gained from DDD. The Orowan relation between *ΔA* and plastic shear strain increment $\Delta\gamma^p$ is used in Eq. (25). In computer simulations, the local plastic shear strain $\Delta\gamma^p$ is transferred from DDD to FEM in order to update the local irradiation defect

density according to Eq. (25). Redistributing $\Delta\gamma^p$ obtained by DDD to the continuum material point is described in detail in our previous work (Cui, Liu et al. 2015, Jamond, Gatti et al. 2016, Liu, Liu et al. 2017).

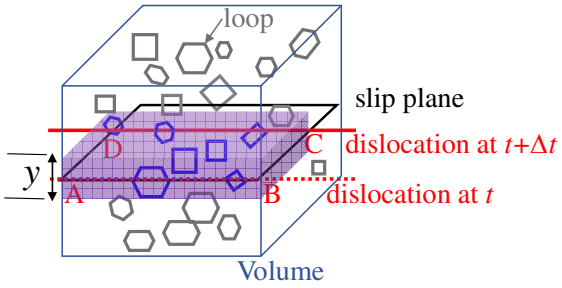

Fig. 4 Interstitial loop damage model. The red line i*s* a dislocation whose slip plane is the plane on points A, B, C and D. The color of loops represents if they are inside(blue) or outside(grey) the capture distance *y* of the dislocation.

2.4.2.2 Kinetic model of voids

To the best of our knowledge, till now there is no well-accepted continuous model that quantitatively describes the evolution of void number density or size due to plastic deformation. Therefore, in the current work, a continuous kinetic model based on atomistic scale studies will be proposed here for the first time. Molecular dynamics simulations show that during the interaction process between a dislocation and a void, the dislocation absorbs vacancies from the void, making the void shrink or even get damaged (Osetsky, Bacon et al. 2003, Terentyev, Bacon et al. 2008, Osetsky and Bacon 2010, Dutta, Bhattacharya et al. 2012), meanwhile forming a jog or a double jog on the dislocation. A void can be completely annihilated after several dislocations pass through it (Osetsky, Bacon et al. 2002). For large voids, Tehranchi and Zhang found that the void lost the outermost vacancies on the compressive glide plane of the dislocation (Tehranchi, Zhang et al. 2017), as described by the red spheres in Fig. 5(a). In this way, the number of lost vacancies in a void is proportional to the void diameter, which is also proportional to the one-third power of the total void volume. Similar phenomena are also observed in the atomistic studies by Osetsky and Bacon (Osetsky and Bacon 2003, Osetsky, Bacon et al. 2003).

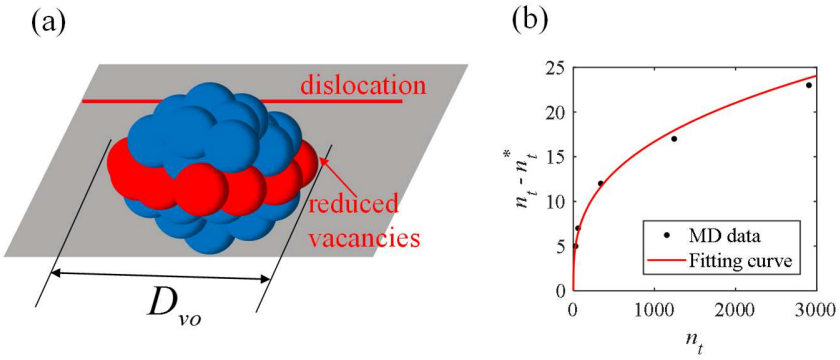

Fig. 5 (a) Interaction between a void and a dislocation line. The red line is a dislocation and red atoms are reduced vacancies. The initial diameter of vacancy is D_{vo}. (b) Removed vacancy number ($n_t - n_t^*$) as a function of initial total vacancy number n_t inside the void. Here, n_t^* is total vacancy number in void after the interaction. MD data comes from ref (Osetsky and Bacon 2003, Osetsky, Bacon et al. 2003). The curve is fitted as $n_t - n_t^* = \alpha (n_t)^{1/3}$ with $\alpha = 1.67$.

Assume that the number of vacancies contained in the void before and after the interaction with the dislocation is n_t and n_t^*, and void diameters before and after the interaction is D_{vo} and D_{vo}^*, respectively. The diameter of a single vacancy is d. By fitting MD data (Osetsky and Bacon 2003, Osetsky, Bacon et al. 2003) shown in Fig. 5 (b), $n_t - n_t^* = \alpha n_t^{1/3}$, and α is determined as 1.67. Combining $n_t \Omega = \pi D_{vo}^3 / 6$, $n_t^* \Omega = \pi \left(D_{vo}^*\right)^3 / 6$ and $\Omega = \pi d^3 / 6$, we can get that when a void interacts with a dislocation once, the relationship between the initial diameter D_{vo} and the updated diameter D_{vo}^* is

$$\left(D_{vo}^*\right)^3 = D_{vo}^{\ 3} - \alpha D_{vo} d^2 \tag{26}$$

To consider the damage effect of voids as a function of plastic strain, assuming that only voids with distance less than $D_{vo}/2$ from the slip plane of the moving dislocation can be cut through, as shown in Fig. 6. If the slip area increment of the dislocation is ΔA, then the proportion of the voids in the interaction is $D_{vo}\Delta A/V$, which is equal to $D_{vo}\Delta\gamma^p/b$, according to Orowan relation. Thus, for the specific control volume V, the reduction of void diameter can be expressed as

$$\Delta D_{vo}^{DDD} = \left(D_{vo}^3 - \frac{\alpha \Delta \gamma^p D_{vo}^2 d^2}{b} \right)^{\frac{1}{3}} - D_{vo} \tag{27}$$

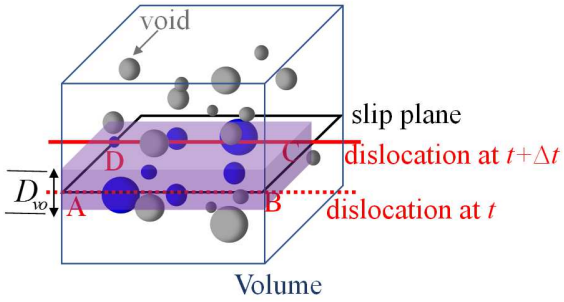

Fig. 6 Void damage model. The red line is a dislocation whose slip plane is plane on points *A*, *B*, *C* and *D*. The color of voids represents if they can interact (blue) or not (grey) with the dislocation. D_{vo} is the average diameter of the void in this volume.

For small voids containing only a few vacancy atoms, dislocations can completely destroy them once they glide through (Tehranchi, Zhang et al. 2017), the void density will decrease. In order to reflect the different damage mechanisms of large and small voids, a critical diameter is defined as $D_{eff}=\left(\alpha d^2\right)^{1/2}$, corresponding to the void diameter $D_{vo}'=\left(D_{vo}^3-\alpha D_{vo}d^2\right)^{1/3}=0$ after one time of interaction.

To sum up, the evolution law of voids is expressed as

$$\begin{cases}\Delta D_{vo}^{DDD}=\left(D_{vo}^3-\dfrac{\alpha\Delta\gamma^p D_{vo}^2 d^2}{b}\right)^{\frac{1}{3}}-D_{vo}, & D_{vo}>D_{eff}\\ \Delta N_{vo}^{DDD}=-N_{vo}\dfrac{D_{vo}\Delta\gamma^p}{b}, & D_{vo}\le D_{eff}\end{cases} \tag{28}$$

Eq. (28) means that voids as small as D_{eff} are entirely destroyed in only one interaction process and thus causing void density to deduce. While for larger ones, interaction only decreases their size.

Finally, the increment of defects (interstitial loops or voids) density ΔN and diameter ΔD in the irradiation defect field is

$$\Delta N=\Delta N^{CD}+\Delta N^{DDD} \tag{29}$$

$$\Delta D=\Delta D^{CD}+\Delta D^{DDD} \tag{30}$$

where ΔN^{CD} and ΔD^{CD} is the increment of defect density and diameter due to irradiation during the interval Δt gained from cluster dynamics.

2.5 Model coupling procedure

In this model, CD handles the nucleation and growth of irradiation defects. DDD calculates the evolution of dislocations. FEM deals with the boundary value problem, and

stores and updates the temporal and spatially heterogeneous information of irradiation defect clusters. The model is concurrently coupled, and DDD and FEM have the same simulation box size.

The parameter transfer procedure between the three models outlined above is shown in Fig. 1. During each CD step, the dislocation density ρ_d is calculated from DDD and transferred to CD to consider the sink effect of dislocations on irradiation defects. Besides, the average defect density and mean size are transferred from FEM to CD as the initial condition for the next CD calculation. In turn, the increment of irradiation defect number density ΔN^{CD} and size ΔD^{CD} obtained by CD is passed to FEM to update the irradiation defect field. At each DDD step, irradiation defect information stored by FEM is interpolated to the quadrature points of the dislocation segment, so as to calculate the resistance stress τ_{irra} that hinders dislocation motion. After dislocations glide, the total slip area of all dislocation segments inside each FEM element is calculated and the corresponding local plastic strain $\Delta\gamma^p$ of each FEM mesh is evaluated as described in detail in our previous work (Cui, Liu et al. 2015). Afterwards, the irradiation defect information stored by FEM is updated according to Eq. (25) and (28) .

A key issue is that the characteristic time scales of DDD and CD are not consistent. The characteristic time increment of DDD is 10^{-12} s, while the typical time increment of cluster dynamics is 10^{-5} s. This huge mismatch makes it almost impossible to perform DDD calculations with the same time scale as that of CD under the current computing resources. In order to solve the problem above, the adiabatic elimination method is used, which is found to be an effective method in dealing with non-linear dynamical systems with vastly different time scales (Lugiato, Mandel et al. 1984). For simultaneous irradiation and mechanical loading, the employed time adaptation method is shown in Fig. 7. Based on the timescale of CD, we firstly calculate CD and advance a specific time increment Δt_{CD}, namely from point A to point C in Fig. 7. During this period, DDD updates the load until the strain reaches the value determined by the target irradiation dose and target mechanical loading, corresponding to a period of Δt_{DDD}. As shown in Fig. 7, Δt_{DDD} is far less than Δt_{CD}, which means that the strain rate in DDD $\dot{\varepsilon}_{DDD}$ is higher than that of the experimental strain rate $\dot{\varepsilon}_{Exp}$. To weaken the strain rate effect, during the rest time interval, namely from point B to point C, no external loading is applied, and only stress relaxation is considered. It is found that Δt_{Relax} is long enough that DDD can continuously run until the dislocation configuration reaches a relatively stable configuration, which is measured according to the variation of the plastic strain rate $\dot{\gamma}^p \le \dot{\gamma}_c^p$. $\dot{\gamma}_c^p$ is the critical small plastic strain rate. Similar treatment is widely used in DDD simulations, and is proved that the simulation results are insensitive to the strain rate (Cui, Po et al. 2017, Cui, Po et al. 2018). Afterward, CD is operated and the next time increment is calculated. This process repeats until the irradiation dose reaches a given value. In summary, we perform a series of quasi-static DDD simulations, evolving adiabatically on the time scale of CD.

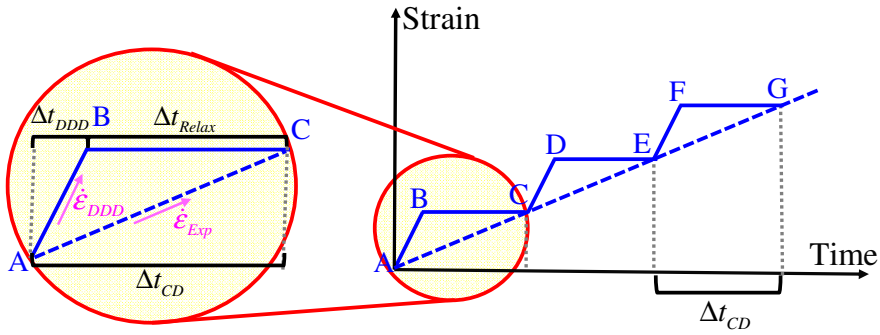

Fig. 7 Time scale adaptation of the model. Δt_{CD} is the time increment for CD simulation. Δt_{DDD} and Δt_{Relax} is time for DDD loading and DDD relaxation in this period. $\dot{\varepsilon}_{DDD}$ is the strain rate used in DDD, and $\dot{\varepsilon}_{Exp}$ is the experimental strain rate.

Note that the proposed model can also be extended to investigate the irradiation creep problem. In this case, dislocation climb plays an important role by directly contributing to the deformation, influencing the irradiation defect cluster evolution, or inducing climb-assisted dislocation glide (Mesarovic 2017, Hayakawa, Okita et al. 2018). In addition, the elastodiffusion of point defects is also important to capture the stress induced preferred absorption mechanism (Woo 1984, Bouobda Moladje, Thuinet et al. 2020). These mechanisms will be further considered in a future dedicated work.

3 Model verification

The model described above can be reduced into a post-irradiation model by first calculating CD to a target dose and then carrying out the sub-coupled model between DDD and FEM. Obviously, the model can also be applied to deal with irradiation or simple mechanical loading problems. Considering that the concurrent irradiation-mechanical loading experiments are very rare, we first use the reduced models and compare their results with the corresponding experimental results to verify the effectiveness of each main part of the model.

3.1 Verification of CD

In order to verify that this model can accurately capture the nucleation and growth of defect clusters during irradiation, we firstly compare our prediction results with the experimental data of irradiated Fe. Here, the evolution of the dislocation density is ignored, and its effect will be considered later. The irradiation temperature T is set to 343 K and the damage production rate G^{NRT} is set to 1×10^{-7} dpa/s. Other input parameters are summarized in Table 2. The values of $\varepsilon_{2v}, \varepsilon_{3v}, \varepsilon_{4v}, \varepsilon_{nv}, \varepsilon_{2i}$ and ε_{3i} are obtained from molecular dynamics description of damage production in displacement cascades (Bacon, Osetsky et al. 2003).

Table 2 Parameters used in cluster dynamics model for irradiated iron.

Type	Symbol	Meaning	Value	Unit	Ref.
Constants	k_B	Boltzmann's constant	8.617×10^{-5}	eV /K	-
Material	b	Burgers vector	2.482×10^{-10}	m	-
	Ω	Atomic volume	1.182×10^{-29}	m^3	-
	ρ_d	Dislocation network density	5×10^{12}	$/m^2$	-
Irradiation	$\varepsilon_{2v}, \varepsilon_{3v}, \varepsilon_{4v}, \varepsilon_{nv}$	The fraction of vacancies produced in the form of di-vacancies, tri-vacancies, tetra-vacancies and immobile vacancies	0.19, 0.11, 0.03, 0.18	1	(Bacon, Osetsky et al. 2003)
	$\varepsilon_{2i}, \varepsilon_{3i}$	The fraction of interstitials produced in the form of di-interstitials and tri-interstitials	0.26,0.19	1	(Bacon, Osetsky et al. 2003)
	η	Cascade efficiency	0.01	1	(Chen, Wei et al. 2019)
	V_{cap}	reciprocal of maximum void density	3.33×10^{-25}	m^3	(Li, Po et al. 2020)
	n_v	the average number of vacancies produced in the form of immobile vacancies	6.1	1	(Bacon, Osetsky et al. 2003)
Energetics	$D_{0,v}$	Vacancy pre-exponential	8.20×10^{-7}	m^2/s	(Jourdan, Bencteux et al. 2014)
	$D_{0,i}$	Interstitial pre-exponential	8.20×10^{-5}	m^2/s	(Soneda and De La Rubia 2001, Meslin, Barbu et al. 2008, Marian and Bulatov 2011)
	$E_v^m, E_{2v}^m, E_{3v}^m, E_{4v}^m$	Migration energy of single vacancies, di-vacancies, tri-vacancies and tetra-vacancies	0.67, 0.62, 0.35, 0.48	eV	(Fu, Torre et al. 2004)
	$E_i^m, E_{2i}^m, E_{3i}^m$	Migration energy of SIAs, di-interstitials and tri-interstitials	0.34, 0.42, 0.43	eV	(Fu, Torre et al. 2004)
	$E_{2v}^b, E_{3v}^b, E_{4v}^b$	Binding energy of di-vacancies, tri-vacancies and tetra-vacancies	0.30, 0.37, 0.62	eV	(Fu, Torre et al. 2004)
	E_{2i}^b, E_{3i}^b	Binding energy of di-interstitials and tri-interstitials	0.83, 0.92	eV	(Fu, Torre et al. 2004)
Interaction	r_{iv}	SIA - vacancy recombination radius	6.5×10^{-9}	m	(Gokhman and Bergner 2010)
	r_{cd}	Trap radius	1.5	b	(Kohnert and Wirth 2015)

$Z_d^i, Z_{il}^i,$ Z_d^v, Z_{il}^v	Dislocation bias factor	1.2, 1.2, 1.0, 1.0	1	(Gokhman and Bergner 2010, Dunn and Capolungo 2015)

Calculation results are shown in Fig. 8. The density of clusters increases rapidly during the initial irradiation stage, which indicates copious cluster nucleation during this period. As the irradiation dose increases, the cluster density gradually reaches equilibrium. This trend of density saturation has been observed in previous work (Meslin, Barbu et al. 2008, Gokhman and Bergner 2010, Chen, Wei et al. 2019) and is consistent with experimental data (Eldrup, Singh et al. 2002, Chen, Wei et al. 2019). Afterward, the growth of defects gradually takes over under irradiation. The density of voids is almost always higher than that of interstitial loops during irradiation, and the saturation of the void density lags behind that of interstitial loops. However, the mean void size is much smaller than that of interstitial loops.

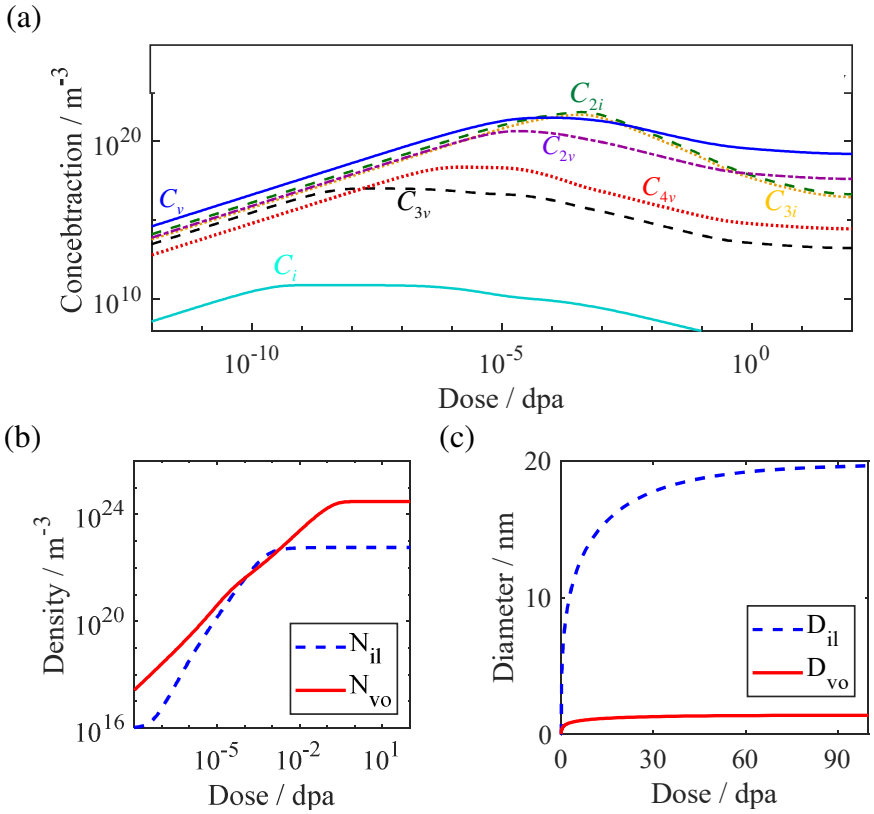

Fig. 8 (a) Evolution of the concentrations of different clusters. (b) Evolution of interstitial loop density N_{il} and void density N_{vo}. (c) Evolution of interstitial loop mean diameter D_{il} and void mean diameter D_{vo}.

The calculated defect density and mean size are compared with the corresponding experimental results in Fig. 9, where different types of defects are distinguished, including interstitial loops and voids. Here, related data for irradiated iron are collected

and listed in Appendix B (Horton, Bentley et al. 1982, Singh, Horsewell et al. 1999, Victoria, Baluc et al. 2000, Eldrup, Singh et al. 2002, Zinkle and Singh 2006, Matijasevic, Lucon et al. 2008, Matijasevic, Van Renterghem et al. 2009, Hernández-Mayoral and Gómez-Briceño 2010, Swenson and Wharry 2015, Chen, Miao et al. 2016, Van Renterghem, Terentyev et al. 2018, Gómez-Ferrer, Dethloff et al. 2020, Zinkle 2020). Generally, the resolution of Transmission Electron Microscopy (TEM) is as small as 1.5-2 nm (Edwards, Simonen et al. 2003, Meslin, Barbu et al. 2008, Hernández-Mayoral and Gómez-Briceño 2010). Positron Annihilation Spectroscopy (PAS) is a more accurate way of observation, but it still cannot observe or accurately measure very small irradiation defects. Therefore, some small defects cannot be observed experimentally and can only be evaluated by computer simulations (Meslin, Barbu et al. 2008). The experimental data on interstitial loops are all based on TEM observations. Because small loops cannot be observed by TEM, the interstitial loop density obtained from experiments lags behind that obtained by CD simulations. However, the nucleation speed of interstitial loops in the simulation and experiments is almost the same (as indicated by the grey arrows in Fig. 9 (a)), indicating the same kinetic process. In addition, the saturation density at different temperatures is also the same, indicating that the results obtained by CD simulation are reliable. For voids, some experimental data are obtained through PAS observations (marked by grey dotted box in Fig. 9(c) and (d)), and the rest are derived from TEM. The void density obtained by CD simulation is closer to the results of PAS, which is also reasonable. Moreover, the average size of interstitial loops and voids obtained by the simulation are in good agreement with the experiment, as shown in Fig. 9(b) and (d). It is found that at a given dose, a higher irradiation temperature leads to larger defects with a smaller density, which is consistent with the experimental observations (Singh, Horsewell et al. 1999, Chen, Miao et al. 2016).

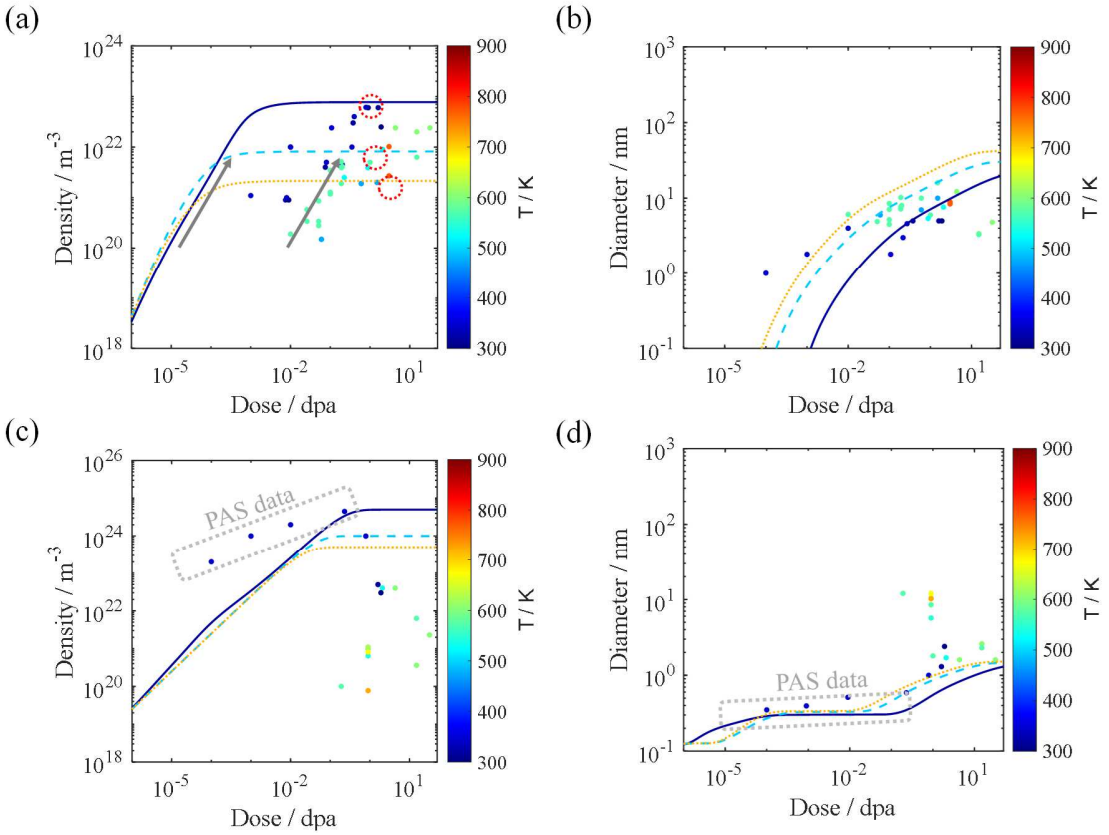

Fig. 9 The evolution of (a) interstitial loop density, (b) interstitial loop diameter, (c) void density and (d) void diameter with irradiation dose at different temperatures in irradiated Fe. The solid lines, dashed lines and dotted lines correspond to the simulation results at temperatures of 300 K, 500 K and 700 K, respectively. The points are obtained from experimental data (Horton, Bentley et al. 1982, Singh, Horsewell et al. 1999, Victoria, Baluc et al. 2000, Eldrup, Singh et al. 2002, Zinkle and Singh 2006, Matijasevic, Lucon et al. 2008, Matijasevic, Van Renterghem et al. 2009, Hernández-Mayoral and Gómez-Briceño 2010, Swenson and Wharry 2015, Chen, Miao et al. 2016, Van Renterghem, Terentyev et al. 2018, Gómez-Ferrer, Dethloff et al. 2020, Zinkle 2020) (see Table A1 in Appendix B for details). The colors of lines and points represent their temperatures.

3.2 Verification of coupled DDD and FEM

In this section, the concurrent model is used as a sequential model by firstly carrying out CD and then performing coupled DDD and FEM, so as to compare with the post-irradiation experiments. Experimental data is obtained from the post-irradiation experiments of Singh and coworkers (Singh, Horsewell et al. 1999). The irradiation dose rate is 3.75×10^{-8} dpa/s, the temperature is 320 K, and the dislocation density is 10^{12} /m^2. With these parameters, CD is firstly computed to the experimental irradiation dose, obtaining the corresponding defect density and size shown in Table 3. Then the coupled DDD and FEM model with these messages as input is carried out, in which the mechanical response and microstructure evolution are computed. The simulated bulk is

2×2×4 μm in size and the strain rate in DDD simulation is 50 /s, which is lower than most of the current DDD simulations.

Table 3 Irradiation defect information from CD, and upper yield strength of post-irradiation from experiment (Singh, Horsewell et al. 1999) and simulation.

	Dose /dpa	0	0.0075	0.075	0.375
Irradiation defects information from CD	Loop density /m^{-3}	0.0	5.44×10^{22}	5.69×10^{22}	5.71×10^{22}
	Loop diameter /nm	0.0	0.80	3.00	5.58
	Void density /m^{-3}	0.0	1.86×10^{23}	1.39×10^{24}	2.86×10^{24}
	Void diameter /nm	0.0	0.29	0.30	0.45
Upper Yield Stress /MPa	Experiment(Singh, Horsewell et al. 1999)	235	275	302	414
	Simulation	167	225	295	376

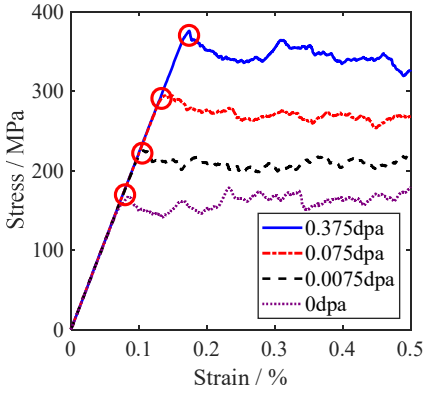

Fig. 10 Computed stress-strain curve of post-irradiated Fe at different irradiation doses. The small red circles are the upper yield points of the four curves.

In both simulation and experiment, the material exhibits irradiation hardening behavior and the yield strength increases with the increase in neutron dose. The calculated upper yield stresses agree well with the experimental data, as shown in Table 3. At a high dose like 0.375 dpa, the stress drops quickly past the yield point as shown in Fig. 10, and a high degree of plastic flow localization occurs (similar to Fig. 12(c)). These trends reproduce the results of experiments (Singh, Horsewell et al. 1999). At the dose level of 0.0075 dpa, there is no indication of the formation of cleared channels. Irradiation defects are evenly distributed in the sample and the deformation behavior of specimens is rather similar to that of the unirradiated ones. This is also consistent with the experiment (Singh, Horsewell et al. 1999).

4 Comparison between coupled irradiation-deformation and post-irradiation conditions

In the following, the developed model will for the first time be used to disclose the underlying mechanisms and different responses between concurrent (coupled) irradiation-deformation and post-irradiation conditions.

4.1 Evolution of irradiation defects

The simulation results of irradiation alone and concurrent irradiation with mechanical loading are compared in Fig. 11. The strain rate is 1.3×10^{-9}/s and irradiation rate is 4.2×10^{-8} dpa/s in the concurrent simulation. It shows that there is no apparent difference in defect density between the two cases at the initial stage of irradiation. Then, interstitial loop density decreases slightly after reaching the saturation stage in the concurrent model. This can be explained by noting that in the irradiation-alone case, the evolution of dislocations is ignored as they just act as stable sinks for irradiation defects. On the other hand, when mechanical loading is simultaneously applied, dislocations glide and interact with defects, and lead to defect damage, thus reducing their density. The size of interstitial loops under the concurrent condition and the irradiation-alone condition is approximately the same, and the void size under the concurrent condition is slightly smaller than that under the irradiation-alone condition.

The conclusion can be drawn that during the irradiation defect nucleation stage, the loss of irradiation defects caused by dislocation movement is very small compared with the density of newly nucleated defects, and the effect of dislocation motion is almost negligible. After the defect density saturates, the damage caused by dislocations gradually dominates, which is manifested as a decrease in defect density. This is because the damage rate of irradiation defects is more significant when the irradiation defect density and size are larger, according to Eq. (25). The size reduction caused by interaction with dislocations is small compared to the growth of the interstitial loop or void due to absorption of mobile defects.

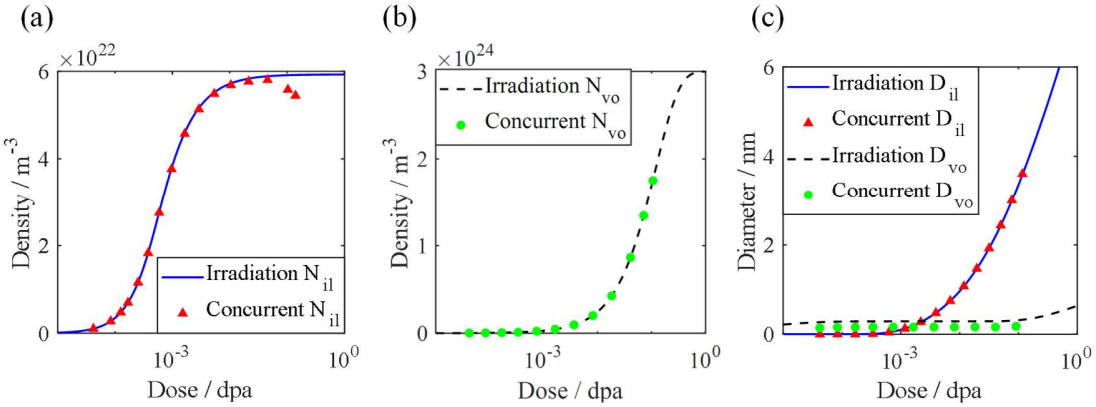

Fig. 11 (a) Interstitial loop density N_{il}, (b) void density N_{vo}, (c) interstitial loop diameter D_{il} and void diameter D_{vo}. 'Irradiation' means irradiation-alone condition, 'Concurrent' means concurrent irradiation and mechanical loading. The strain rate is 1.3×10^{-9}/s and irradiation rate is 4.2×10^{-8} dpa/s in the concurrent simulation.

4.2 Mechanical response and microscopic insights

The model developed here leads to the possibility of understanding the difference in the mechanical response of materials where the mechanical loading is applied post-irradiation or concurrently with irradiation. For the post-irradiation case, the specimen is first irradiated to a target dose (1 dpa) and then undergoes mechanical deformation without irradiation. On the other hand, the specimen is simultaneously subjected to an irradiation dose rate $\dot{I}$ and an applied strain rate of $\dot{\varepsilon}=1.3\times10^{-7}$/s at the same time for the concurrent irradiation-deformation case. A rather low strain rate is chosen, consistent with the relevant experiment (Singh, Edwards et al. 2004). The irradiation dose rate $\dot{I}$ is set as 4.2×10^{-8} dpa/s, 4.2×10^{-7} dpa/s and 4.2×10^{-6} dpa/s for concurrent simulations. Unirradiated cases are also calculated for comparison. Note that for post-irradiation cases, the stress-strain curve corresponds to a given irradiation dose, while for the concurrent modeling, the irradiation dose increases with an increase of the strain. To eliminate the influence of initial dislocation microstructures, five specimens of size 1.5×1.5×3 μm with different initial configurations were simulated and the mechanical response is averaged, as shown in Fig. 12(a). The insensitivity of the simulation results to the simulation box size is discussed in Appendix C.

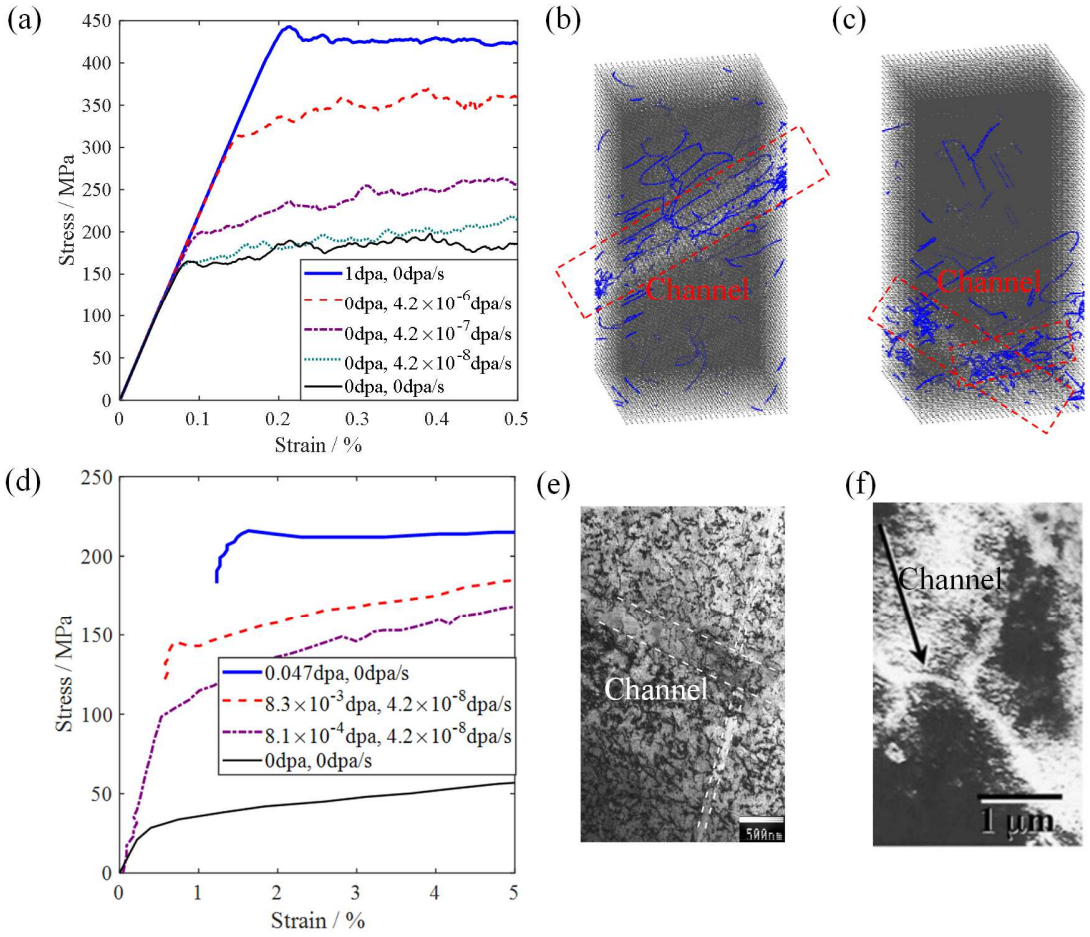

Fig. 12 Stress-strain curves of unirradiated, post-irradiated and in-reactor materials from (a) simulations of Fe and (d) experiments of Cu (Singh, Edwards et al. 2004). The first and second parameters in the legend of (a, d) represent the irradiation dose before loading and the irradiation dose rate during loading. The irradiation defect distribution obtained by simulation in (b) concurrent case with an irradiation rate of 4.2×10^{-6} dpa/s when the strain reaches 0.82% and (c) post irradiation case when the strain reaches 0.87% (the symbol size is proportional to the local irradiation defect density). Blue lines in (b, c) are dislocations. (e, f) Dislocation channels observed for concurrent (Singh, Edwards et al. 2004) and post-irradiation case from experiment (Zinkle and Singh 2006). Channels are framed by dashed lines in (b-c, e) and indicated by arrows in (f).

Our simulation results reproduce several features that agree well with the available experimental observations (Singh, Edwards et al. 2004). Firstly, in Fig. 12 (a) it is clear that the hardening effect occurs in the concurrent irradiation-mechanical loading condition, similar to the previous experiment shown in Fig. 12 (d) (Singh, Edwards et al. 2004). There is no apparent yield drop (softening) in concurrent simulation, while plastic flow localization and dislocation channel formation still occur in the sample, as shown in Fig. 12 (b) and (e). Secondly, for post-irradiation, samples show a significant yield drop in both experiment and simulation, accompanied with the formation of dislocation channels, as shown in Fig. 12 (c) and (f).

What determines the material performance (hardening or plastic instability) under the simultaneous loading and irradiation conditions? It is found that post-yield behavior is a result of a competition between hardening due to dislocation multiplication and irradiation defect nucleation and growth, and softening due to dislocation-induced defect damage. If dislocations glide many times within a specific region, the induced destruction of irradiation defects gradually leads to the formation of a dislocation channel (or very low irradiation defect density region). These act as positions with lower irradiation defect barrier, so most of the subsequent deformation concentrates in a heterogeneous manner, resulting in highly localized plasticity.

The dominated different microstructure evolution processes under concurrent irradiation-mechanical loading and post-irradiation conditions can be clearly seen in Fig. 13. Here, the evolution of interstitial loop density N_{il} is taken as an example to illustrate the basic evolution trend of irradiation defects under these two cases. The reported results in Fig. 13 are averages over ten random points inside the dislocation channels and ten random points outside the dislocation channel. It is found that during post-irradiation tests, the reduction rate of N_{il} is much higher inside the dislocation channel, compared with that in the outside region (see Fig. 13 (a)). Therefore, the barrier effect induced by irradiation defects quickly reduces inside the dislocation channel. Accompanied with the appearance of plastic deformation localization inside dislocation channel, an obvious yield drop is observed (see Fig. 12 (a)). In contrast, during concurrent irradiation-deformation conditions shown in Fig. 13 (b), the appearance of dislocation channel is not accompanied with the yield drop. For positions outside dislocation channel, the density of new irradiation defects rapidly increases at the initial stage of irradiation, which hinders dislocation glide. At the later stages of irradiation, the increase rate of N_{il} reduces, and a saturation stage of N_{il} may be gradually achieved. N_{il} keeps increasing during the considered deformation stage, suggesting it is dominated by the irradiation process and can continuously contribute to the hardening behavior. For points inside dislocation channel, N_{il} also firstly increases. When the material reaches the yield point, both the defect density inside and outside the channel increases, as marked by the blue circle in Fig. 13(b), so yield drop will not occur immediately after yielding for concurrent irradiation-deformation condition. When the irradiation defects reach a high density and large size, the damage rate of irradiation defects induced by dislocation motion becomes more obvious, according to Eq. (25) and (28). Therefore, when N_{il} inside dislocation channel reaches a relatively high value, it exhibits a wavelike decrease as a result of the competition between continuous defects nucleation and growth due to concurrent irradiation, and the defect damage due to plastic deformation. As a result, the material remains to exhibit an overall hardening behavior. However, with the difference between N_{il} inside dislocation channel and N_{il} outside dislocation channel becoming more apparent, a dislocation channel can be gradually observed, promoting plastic flow localization and the further development of dislocation channel.

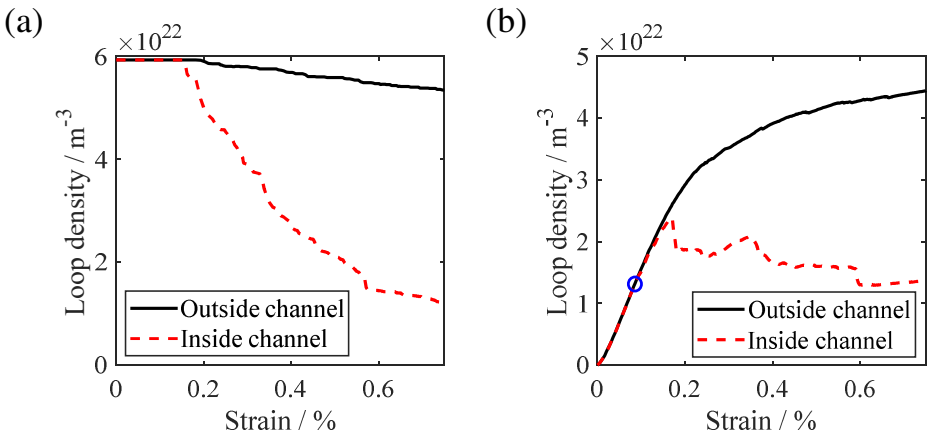

Fig. 13 Evolution of interstitial loop density N_{il} during (a) post-irradiation test and (b) concurrent irradiation-deformation test corresponding to irradiation dose rate 4.2×10^{-8} dpa/s in Fig. 12. The small blue circle in (b) corresponds to the yield point. Results are averages over randomly chosen 10 points outside and 10 points inside the dislocation channel.

5 Summary and Conclusions

A concurrent irradiation-mechanical coupling model is proposed and established to study the mechanical response and internal physical mechanisms of irradiated materials. Compared with traditional post-irradiation studies, this model for the first time leads to the opportunity to disclose the collective dynamics of irradiation defects and dislocations under coupled irradiation and mechanical loading conditions. This, in turn allows studies of plastic flow of irradiated structural materials during in-reactor service conditions.

The model concurrently couples irradiation-induced defect cluster dynamics, discrete dislocation dynamics, and the finite element methods. The time scale mismatch problem is solved by proposing a time marching scheme that adiabatically eliminates fast dislocation glide motion, treating glide dynamics as a series of quasi-static configurations. The spatial scale mismatch problem and computation efficiency difficulties are overcome by developing the discrete-continuous coupled method. In particular, this work developed the continuous model to describe the coupled irradiation hardening induced by interstitial loops and voids, and for the first time includes a kinetic model reproducing the interaction between voids and dislocations. The number of vacancies lost by a dislocation gliding through a void is proportional to the diameter of the void. These sub-models can also be directly used in larger scale continuous models, such as crystal plasticity or the finite element calculations.

The proposed model can be directly reduced into an irradiation defect dynamics model alone. Therefore, it can be carefully calibrated by rich experimental data about the irradiation defect kinetics. The predicted results agree well with the corresponding results of the nucleation and growth of defects during irradiation. In addition, this model can also

be directly reduced to a post-irradiation model and compared with previous post-irradiation experiments. The predicted yield strength and microstructure characteristics agree well with available experimental results, thus verifying the overall reliability of the integrated model.

The developed model is used to disclose the difference in microstructure evolution and mechanical response under post-irradiation conditions, as well as concurrent irradiation-deformation coupling conditions. The prediction results agree well with available experimental results. Irradiation hardening is observed under both conditions, but the correlation between dislocation channel formation and the obvious yield drop is only observed in samples tested post-irradiation, but not observed under concurrent irradiation-deformation conditions. New insights into the coupled kinetics of irradiation defects, dislocations and the mechanical response are disclosed under these conditions. The difference between post-irradiation and in-reactor tests is explained based on these studies. Hardening and plastic instability result from competition among multiple mechanisms, like dislocation multiplication, irradiation defect generation, growth and damage.

The model presented in the current work leads to a new opportunity to understand the mechanical behavior of in-reactor materials. It can also be used to study simple irradiation, post-irradiation, and complicated multi-physics problems, providing a powerful tool for subsequent research and guiding the design of expensive irradiation experiments.

Appendix A

To obtain the denominator's value in the expression of the 1D migrating case, namely m in Eq.(9), the interaction energy between a dislocation loop and a dislocation line (Makin 1964, Golubov, Barashev et al. 2015) is calculated. It shows that for an edge dislocation line lying on a $<1\bar{1}0>$ plane with the Burgers vector <111> interacting with dislocation loops with Burgers vector <111>, $<\bar{1}11>$, $<1\bar{1}1>$ or $<11\bar{1}>$, the corresponding trapping zone for dislocation loops with Burgers vector <111> is more extensive than the other three cases, as shown in Fig. A1. Besides, the trapping zones for screw dislocations are smaller than those for edge dislocations. It concludes that the sink strength for small clusters with a given Burgers vector direction mainly depends on the density of dislocations of the same Burgers vector only. Therefore, m=4.

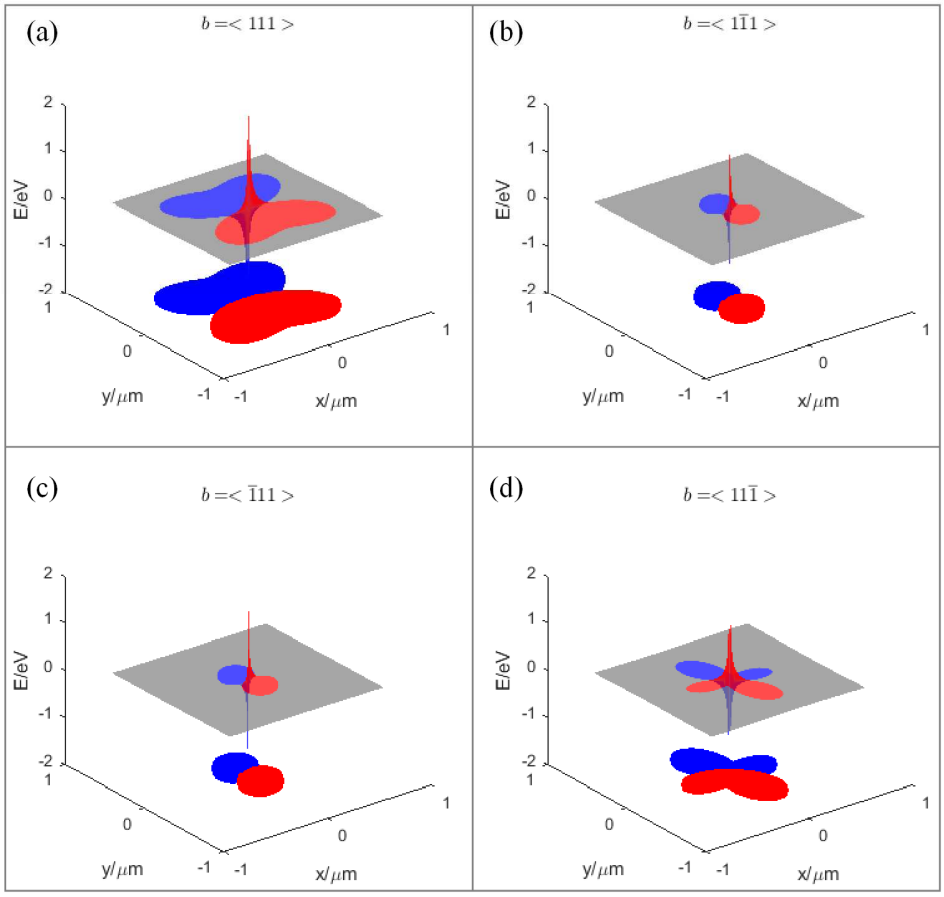

Fig. A1 The interaction energy of an edge dislocation line lying on $<1\bar{1}0>$ plane with Burgers vector $<111>$ interacting with a dislocation loop size 1 nm. Burger vector of dislocation is shown in the subgraph. Each subgraph shows three regions: the capture zone (blue) where $E<-k_BT$, the repulsion zone (red) where $E>-k_BT$, and an intermediate area where $E\approx 0$ (gray).

Appendix B

Table A1 Experimental irradiation defect data of iron and relevant alloys.

Material	Irradiation	Energy	Dpa /s	T /K	Dose/dpa	Type1	N1 /m3	D1 /nm	Type2	N2 /m3	D2 /nm	Ref.
Pure Fe	neutron	>1MeV	3.75×10^{-8}	320	0.0075	cluster	9.00×10^{20}					(Singh, Horsewell et al. 1999)
Pure Fe	neutron	>1MeV	3.75×10^{-8}	320	0.075	cluster	4.00×10^{21}					(Singh, Horsewell et al. 1999)
Pure Fe	neutron	>1MeV	3.75×10^{-8}	320	0.375	cluster	3.00×10^{22}	5				(Singh, Horsewell et al. 1999)
Pure Fe	neutron	5e23n/m2	3.75×10^{-8}	523	0.225	cluster	2.50×10^{21}					(Singh, Horsewell et al. 1999)
Pure Fe	neutron	14MeV		300	0.009	cluster	9.00×10^{20}					(Zinkle 2020)
Pure Fe	neutron	14MeV		300	0.01	cluster	1.0×10^{22}					(Zinkle 2020)
Pure Fe	neutron	14MeV		300	0.9	cluster	6.0×10^{22}					(Zinkle 2020)
Pure Fe	neutron	> 1 MeV	7.00×10^{-7}	343	0.0001	loop		1	void	2.00×10^{23}	0.35	(Eldrup, Singh et al. 2002, Zinkle and Singh 2006)
Pure Fe	neutron	> 1 MeV	7.00×10^{-7}	343	0.001	loop	1.10×10^{21}	1.8	void	1.00×10^{24}	0.395	(Eldrup, Singh et al. 2002, Zinkle and Singh 2006)
Pure Fe	neutron	> 1 MeV	7.00×10^{-7}	343	0.01	loop	1.00×10^{22}	4	void	2.00×10^{24}	0.513	(Eldrup, Singh et al. 2002, Zinkle and Singh 2006)
Pure Fe	neutron	> 1 MeV	7.00×10^{-7}	343	0.23				void	4.50×10^{24}	0.589	(Eldrup, Singh et al. 2002, Zinkle and Singh 2006)
Pure Fe	neutron	> 1 MeV	7.00×10^{-7}	343	0.79	loop	6.10×10^{22}		void	1.00×10^{24}	1	(Eldrup, Singh et al. 2002, Zinkle and Singh 2006)
Pure Fe				340	0.2	loop	4.50×10^{21}					(Zinkle and Singh 2006)
Pure Fe				340	0.35	loop	1.00×10^{22}					(Zinkle and Singh 2006)
Pure Fe				340	0.008	loop	1.00×10^{21}					(Zinkle and Singh 2006)
Pure Fe				340	0.08	loop	5.00×10^{21}					(Zinkle and Singh 2006)
Pure Fe				340	0.4	loop	4.00×10^{22}					(Zinkle and Singh 2006)
Pure Fe	neutron			573	0.01	loop	1.90×10^{20}	6.1				(Chen, Miao et al. 2016)
Pure Fe	neutron			573	0.1	loop	1.20×10^{21}	8.5				(Chen, Miao et al. 2016)
Pure Fe	neutron			573	1	loop	5.00×10^{21}	6	void		1.8	(Chen, Miao et al. 2016)
Pure Fe	neutron			573	0.026	loop	3.40×10^{20}					(Hernández-Mayoral and Gómez-Briceño 2010)
Pure Fe	neutron			573	0.051	loop	8.60×10^{20}	4.9				(Hernández-Mayoral and Gómez-Briceño 2010)
Pure Fe	neutron			573	0.1	loop	1.28×10^{21}	7.1				(Hernández-

											Mayoral and Gómez-Briceño 2010)
Pure Fe	neutron			573	0.19	loop	3.91×10^{21}	10.2	void	1.00×10^{20}	12	(Hernández-Mayoral and Gómez-Briceño 2010)
Pure Fe	neutron			573	0.2	loop	4.10×10^{21}	8				(Matijasevic, Van Renterghem et al. 2009)
Pure Fe	neutron	>0.1 MeV		548	~0.9				void	6.4×10^{20}	5.7	(Horton, Bentley et al. 1982)
Pure Fe	neutron	>0.1 MeV		573					void	9.8×10^{20}	8.5	(Horton, Bentley et al. 1982)
Pure Fe	neutron	>0.1 MeV		623					void	11×10^{20}	10.5	(Horton, Bentley et al. 1982)
Pure Fe	neutron	>0.1 MeV		673					void	8.2×10^{20}	12.0	(Horton, Bentley et al. 1982)
Pure Fe	neutron	>0.1 MeV		723					void	0.77×10^{20}	10.2	(Horton, Bentley et al. 1982)
Fe-0.1Cu	neutron			573	0.026	loop	5.80×10^{20}					(Hernández-Mayoral and Gómez-Briceño 2010)
Fe-0.1Cu	neutron			573	0.051	loop	2.80×10^{20}					(Hernández-Mayoral and Gómez-Briceño 2010)
Fe-0.1Cu	neutron			573	0.1	loop	1.18×10^{21}	4.5				(Hernández-Mayoral and Gómez-Briceño 2010)
Fe-0.1Cu	neutron			573	0.19	loop	1.90×10^{21}	7.7				(Hernández-Mayoral and Gómez-Briceño 2010)
Fe-0.3Cu	neutron			573	0.051	loop	3.40×10^{20}					(Hernández-Mayoral and Gómez-Briceño 2010)
Fe-0.3Cu	neutron			573	0.1	loop	3.47×10^{21}	5.2				(Hernández-Mayoral and Gómez-Briceño 2010)
Fe-0.3Cu	neutron			573	0.19	loop	5.13×10^{21}	7.2				(Hernández-Mayoral and Gómez-Briceño 2010)
Fe9%Cr ODS steel	neutron			773	3	loop	2.70×10^{21}	8.9	void	2.40×10^{20}	3.46	(Swenson and Wharry 2015)
Fe9%Cr ODS steel	proton			773	3	loop	1.02×10^{22}	8.4	void	3.40×10^{21}	4	(Swenson and Wharry 2015)
Eurofer97	neutron	>0.1MeV	8.05×10^{-7}	603	15	loop	2.00×10^{22}	3.4	void	3.60×10^{20}	2.6	(Gómez-Ferrer, Dethloff et al. 2020)
Eurofer97	neutron	>0.1MeV	2.25×10^{-7}	573	15	loop	6.30×10^{21}	3.3	void	6.30×10^{21}	2.3	(Gómez-Ferrer, Dethloff et al. 2020)
Eurofer97	neutron	>0.1MeV	8.05×10^{-7}	603	32	loop	2.40×10^{22}	4.8	void	2.30×10^{21}	1.6	(Gómez-Ferrer, Dethloff et al. 2020)
Eurofer97	neutron			573	0.06	loop	1.5×10^{20}	6				(Matijasevic, Lucon

												et al. 2008)
Eurofer97	neutron			573	0.6	loop	1.9×10^{21}	10				(Matijasevic, Lucon et al. 2008)
Eurofer97	neutron			573	1.5	loop	2.0×10^{21}	16				(Matijasevic, Lucon et al. 2008)
T91 steel	n+p	8.5MeV		527	0.88	loop	3.90×10^{21}	5.4				(Van Renterghem, Terentyev et al. 2018)
T91 steel	n+p	8.5MeV		533	2.07	loop	9.00×10^{21}	7.6	void	4.00×10^{22}	1.7	(Van Renterghem, Terentyev et al. 2018)
T91 steel	n+p	8.5MeV		603	4.35	loop	2.40×10^{22}	12.2	void	4.00×10^{22}	1.6	(Van Renterghem, Terentyev et al. 2018)
T91 steel	neutron			473	0.06	loop	1.5×10^{20}	6				(Matijasevic, Lucon et al. 2008)
T91 steel	neutron			473	0.6	loop	1.9×10^{21}	7				(Matijasevic, Lucon et al. 2008)
T91 steel	neutron			473	1.5	loop	2.0×10^{21}	10				(Matijasevic, Lucon et al. 2008)
Fe-9Cr	neutron	Fission	9.40×10^{-8}	315	1.6	Iloop	2×10^{20}-1.2×10^{23}	5	void	1.7×10^{22}~8.2×10^{22}	1.3	(Haley, de Moraes Shubeita et al. 2020)
Fe-9Cr	proton	1.2MeV	1.00×10^{-5}	302	1.9	Iloop	2.5×10^{22}	5	void	3×10^{22}	2.4	(Haley, de Moraes Shubeita et al. 2020)
A508-3	proton		1.00×10^{-5}	353	0.108	loop	2.4×10^{22}	1.8				(Lei, Ding et al. 2014)
A508-3	proton		1.00×10^{-5}	353	0.216	loop	2.5×10^{22}	3				(Lei, Ding et al. 2014)
A508-3	proton		1.00×10^{-5}	353	0.271	loop	2.7×10^{22}	4.6				(Lei, Ding et al. 2014)

Experimental data of irradiation defects of iron and relevant alloy in different working conditions are summarised in Table A1. Globally, the dislocation loop density is in the range of 10^{20}~10^{23} m^{-3} with a size ranging from 2 nm to 10 nm in studied conditions (dose < 3 dpa, irradiation temperature < 700 K). For a given irradiation temperature, it is seen that increasing irradiation dose results in a higher loop density and a larger loop size. Alternatively, a higher irradiation temperature induces a smaller loop density but a larger loop size. Alloying elements such as Cu and Cr will not significantly influence the loop density and loop size at this low dose and low irradiation temperature regime.

Moreover, it was shown that in irradiated iron, the irradiation-induced dislocation loops consist of <111> and <100> loops. The ratio of <111> to <100> loops is primarily dependent on irradiation dose and temperature. <111> loops are the predominant feature in samples irradiated at low temperature and low dose. At intermediate temperature (> 700 K) or a large dose, <100> loops become the dominant defect.

Appendix C

In order to further verify the effectiveness of the model, larger specimens (2×2×4 μm) with different initial configurations are calculated, as shown in Fig. A2. The initial dislocation configurations of the samples in Fig. A2 (a), (b) and (c) are dislocation sources with an average length of 200 nm, 300 nm and 400 nm, respectively. Results in Fig. A2 (a), (b) and (c) are all in good agreement with the experiment(Singh, Edwards et al. 2004), and there is no obvious difference between them. It proves that there is no obvious sample size effect or dislocation source size effect in this simulation.

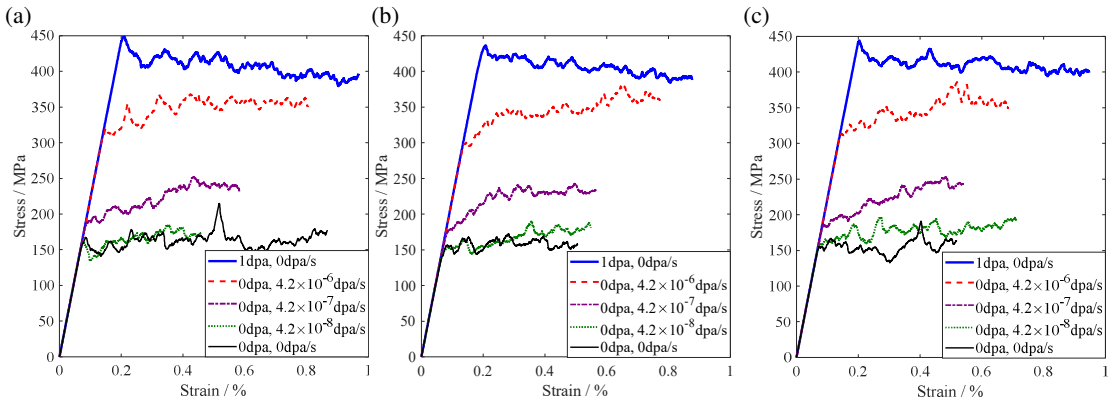

Fig. A2 Stress-strain curve from samples of 2×2×4 μm and average dislocation source size of (a) 200 nm (b) 300 nm and (c) 400 nm.

Acknowledgment:

This material is based upon work supported by the National Natural Science Foundation of China under Grant No.12172194, 11972208, 11921002, and Tsinghua University Initiative Scientific Research Program. N.G. and Y.L. would like to acknowledge the support of the US Department of Energy (DOE), grant number DE-SC0018410 with UCLA.

References:

Akhondzadeh, S., R. B. Sills, N. Bertin and W. Cai (2020). "Dislocation density-based plasticity model from massive discrete dislocation dynamics database." Journal of the Mechanics and Physics of Solids 145: 104152.

Alawadi, A. and H. Abdolvand (2020). "Measurement and modeling of micro residual stresses in zirconium crystals in three dimension." Journal of the Mechanics and Physics of Solids 135: 103799.

Arsenlis, A., M. Rhee, G. Hommes, R. Cook and J. Marian (2012). "A dislocation dynamics study of the transition from homogeneous to heterogeneous deformation in irradiated body-centered cubic iron." Acta Materialia 60(9): 3748-3757.

Aubry, S., M. Rhee, G. Hommes, V. V. Bulatov and A. Arsenlis (2016). "Dislocation dynamics in hexagonal close-packed crystals." Journal of the Mechanics and Physics of Solids 94: 105-126.

Bacon, D. J., U. F. Kocks and R. O. Scattergood (1973). "The effect of dislocation self-interaction on the orowan stress." Philosophical Magazine 28(6): 1241-1263.

Bacon, D. J. and Y. N. Osetsky (2005). "Modelling dislocation–obstacle interactions in metals exposed to an irradiation environment." Materials Science and Engineering: A 400-401: 353-361.

Bacon, D. J., Y. N. Osetsky, R. Stoller and R. E. Voskoboinikov (2003). "MD description of damage production in displacement cascades in copper and α-iron." Journal of Nuclear Materials 323(2-3): 152-162.

Balbuena, J. P., M. J. Aliaga, I. Dopico, M. Hernández-Mayoral, L. Malerba, I. Martin-Bragado and M. J. Caturla (2019). "Insights from atomistic models on loop nucleation and growth in α-Fe thin films under Fe+ 100 keV irradiation." Journal of Nuclear Materials 521: 71-80.

Barbu, A. and E. Clouet (2007). "Cluster dynamics modeling of materials: advantages and limitations." Solid State Phenom 129: 51-58.

Barton, N. R., A. Arsenlis and J. Marian (2013). "A polycrystal plasticity model of strain localization in irradiated iron." Journal of the Mechanics and Physics of Solids 61(2): 341-351.

Beeler, B., M. Asta, P. Hosemann and N. Grønbech-Jensen (2015). "Effects of applied strain on radiation damage generation in body-centered cubic iron." Journal of Nuclear Materials 459: 159-165.

Bergner, F., C. Pareige, M. Hernández-Mayoral, L. Malerba and C. Heintze (2014). "Application of a three-feature dispersed-barrier hardening model to neutron-irradiated Fe–Cr model alloys." Journal of Nuclear Materials 448(1-3): 96-102.

Bouobda Moladje, G. F., L. Thuinet, C. Domain, C. S. Becquart and A. Legris (2020). "Phase-field calculations of sink strength in Al, Ni, and Fe: A detailed study of elastic effects." Computational Materials Science 183: 109905.

Byun, T. S., K. Farrell and M. Li (2008). "Deformation in metals after low-temperature irradiation: Part II – Irradiation hardening, strain hardening, and stress ratios." Acta Materialia 56(5): 1056-1064.

Byun, T. S. and N. Hashimoto (2006). "Strain Localization in Irradiated Materials." Nuclear Engineering and Technology 38: 619-638.

Chen, C., Y. Wei, L. Guo, W. Zhang and Y. Yu (2019). "Rate theory study of the proton-irradiation induced dislocation loops in modified 310S steels." Nuclear Instruments and Methods in Physics Research Section B: Beam Interactions with Materials and Atoms 461: 181-185.

Chen, L., W. Liu, L. Yu, Y. Cheng, K. Ren, H. Sui, X. Yi and H. Duan (2020). "Probabilistic and constitutive models for ductile-to-brittle transition in steels: A competition between cleavage and ductile fracture." Journal of the Mechanics and Physics of Solids 135: 103809.

Chen, W.-Y., Y. Miao, J. Gan, M. A. Okuniewski, S. A. Maloy and J. F. Stubbins (2016). "Neutron irradiation effects in Fe and Fe-Cr at 300 °C." Acta Materialia 111: 407-416.

Cui, W., Y. Cui and W. Liu (2021). "A statistical model of irradiation hardening induced by non-periodic irradiation defects." Scripta Materialia 201: 113959.

Cui, Y., N. Ghoniem and G. Po (2021). "Plasticity of irradiated materials at the nano and micro-scales." Journal of Nuclear Materials 546: 152746.

Cui, Y., Z. Liu and Z. Zhuang (2015). "Quantitative investigations on dislocation based discrete-continuous model of crystal plasticity at submicron scale." International Journal of Plasticity 69: 54-72.

Cui, Y., G. Po and N. Ghoniem (2017). "Does irradiation enhance or inhibit strain bursts at the submicron scale?" Acta Materialia 132: 285-297.

Cui, Y., G. Po and N. Ghoniem (2018). "Size-Tuned Plastic Flow Localization in Irradiated Materials at the Submicron Scale." Physical Review Letters 120(21): 215501.

Cui, Y., G. Po and N. Ghoniem (2018). "Suppression of Localized Plastic Flow in Irradiated Materials." Scripta Materialia 154: 34-39.

Cui, Y., G. Po and N. M. Ghoniem (2018). "A coupled dislocation dynamics-continuum barrier field model with application to irradiated materials." International Journal of Plasticity 104: 54-67.

De la Rubia, T. D., H. M. Zbib, T. A. Khraishi, B. D. Wirth, M. Victoria and M. J. Caturla (2000). "Multiscale modelling of plastic flow localization in irradiated materials." Nature 406: 871-874.

Dunn, A., L. Agudo-Merida, I. Martin-Bragado, M. McPhie, M. Cherkaoui and L. Capolungo (2014). "A novel method for computing effective diffusivity: Application to helium implanted α-Fe thin films." Journal of Nuclear Materials 448(1-3): 195-205.

Dunn, A. and L. Capolungo (2015). "Simulating radiation damage accumulation in α-Fe: A spatially resolved stochastic cluster dynamics approach." Computational Materials Science 102: 314-326.

Dunn, A., R. Dingreville and L. Capolungo (2016). "Multi-scale simulation of radiation damage accumulation and subsequent hardening in neutron-irradiated α-Fe." Modelling and Simulation in Materials Science and Engineering 24(1): 015005.

Dunn, A., B. Muntifering, R. Dingreville, K. Hattar and L. Capolungo (2016). "Displacement rate and temperature equivalence in stochastic cluster dynamics simulations of irradiated pure α-Fe." Journal of Nuclear Materials 480: 129-137.

Dunn, A. Y., L. Capolungo, E. Martinez and M. Cherkaoui (2013). "Spatially resolved stochastic cluster dynamics for radiation damage evolution in nanostructured metals." Journal of Nuclear Materials 443(1-3): 128-139.

Dutta, A., M. Bhattacharya, N. Gayathri, G. C. Das and P. Barat (2012). "The mechanism of climb in dislocation–nanovoid interaction." Acta Materialia 60(9): 3789-3798.

Edwards, D. J., E. P. Simonen, F. A. Garner, L. R. Greenwood, B. M. Oliver and S. M. Bruemmer (2003). "Influence of irradiation temperature and dose gradients on the microstructural evolution in neutron-irradiated 316SS." Journal of Nuclear Materials 317(1): 32-45.

Eldrup, M., B. N. Singh, S. J. Zinkle, T. S. Byun and K. Farrell (2002). "Dose dependence of defect accumulation in neutron irradiated copper and iron." Journal of Nuclear Materials 307–311: 912-917.

Fan, C., R. G. S. Annadanam, Z. Shang, J. Li, M. Li, H. Wang, A. El-Azab and X. Zhang (2020). "Irradiation induced void spheroidization, shrinkage and migration in Cu at elevated temperatures: An in situ study." Acta Materialia 201: 504-516.

Fan, H., Q. Wang, J. A. El-Awady, D. Raabe and M. Zaiser (2021). "Strain rate dependency of dislocation plasticity." Nat Commun 12(1): 1845.
Fan, Y., A. Kushima, S. Yip and B. Yildiz (2011). "Mechanism of void nucleation and growth in bcc Fe: atomistic simulations at experimental time scales." Physical Review Letters 106(12): 125501.
Fu, C.-C., J. D. Torre, F. Willaime, J.-L. Bocquet and A. Barbu (2004). "Multiscale modelling of defect kinetics in irradiated iron." Nature Materials 4(1): 68-74.
Garner, F. A., M. L. Hamilton, N. F. Panayotou and G. D. Johnson (1981). "The microstructural origins of yield strength changes in aisi 316 during fission or fusion irradiation." Journal of Nuclear Materials 104: 803-808.
Garud, Y. S. (2016). "Low temperature creep and irradiation creep in nuclear reactor applications: A critical review." International Journal of Pressure Vessels and Piping 139-140: 137-145.
Geslin, P.-A., R. Gatti, B. Devincre and D. Rodney (2017). "Implementation of the nudged elastic band method in a dislocation dynamics formalism: Application to dislocation nucleation." Journal of the Mechanics and Physics of Solids 108: 49-67.
Ghoniem, N. M. (1989). "Stochastic theory of diffusional planar-atomic clustering and its application to dislocation loops." Physical Review B 39(16): 11810-11819.
Ghoniem, N. M., J. N. Alhajji and F. A. Garner (1992). Hardening of Irradiated Alloys due to the Simultaneous Formation of Vacancy and Interstitial Loops. Effect of Radiation On Materials: Eleventh Conference, ASTM STP 782: 1054-1072.
Ghoniem, N. M., S.-H. Tong, B. N. Singh and L. Z. Sun (2001). "On dislocation interaction with radiation-induced defect clusters and plastic flow localization in fcc metals." Philosophical Magazine A 81(11): 2743-2764.
Ghoniem, N. M., S.-H. Tong and L. Z. Sun (2000). "Parametric dislocation dynamics: A thermodynamics-based approach to investigations of mesoscopic plastic deformation." Physical Review B 61(2): 913.
Gilbert, M. R., Z. Yao, M. A. Kirk, M. L. Jenkins and S. L. Dudarev (2009). "Vacancy defects in Fe: Comparison between simulation and experiment." Journal of Nuclear Materials 386-388: 36-40.
Gokhman, A. and F. Bergner (2010). "Cluster dynamics simulation of point defect clusters in neutron irradiated pure iron." Radiation Effects and Defects in Solids 165(3): 216-226.
Golubov, S. I., A. V. Barashev and R. E. Stoller (2012). Radiation Damage Theory. Comprehensive Nuclear Materials: 357-391.
Golubov, S. I., A. V. Barashev, R. E. Stoller and B. N. Singh (2015). Breakthrough in Understanding Radiation Growth of Zirconium. Zirconium in the Nuclear Industry: 17th Volume: 729-758.
Gómez-Ferrer, B., C. Dethloff, E. Gaganidze, L. Malerba, C. Hatzoglou and C. Pareige (2020). "Nano-hardening features in high-dose neutron irradiated Eurofer97 revealed by atom-probe tomography." Journal of Nuclear Materials 537: 152228.
Gu, Y., J. Han, S. Dai, Y. Zhu, Y. Xiang and D. J. Srolovitz (2017). "Point defect sink efficiency of low-angle tilt grain boundaries." Journal of the Mechanics and Physics of Solids 101: 166-179.
Haley, J. C., S. de Moraes Shubeita, P. Wady, A. J. London, G. R. Odette, S. Lozano-Perez and S. G. Roberts (2020). "Microstructural examination of neutron, proton and self-ion irradiation damage in a model Fe9Cr alloy." Journal of Nuclear Materials 533: 152130.
Hayakawa, S., T. Okita, M. Itakura, M. Aichi and K. Suzuki (2018). "Interactions between clusters of self-interstitial atoms via a conservative climb in BCC–Fe." Philosophical Magazine 98(25): 2311-2325.
Hernández-Mayoral, M. and D. Gómez-Briceño (2010). "Transmission electron microscopy study on neutron irradiated pure iron and RPV model alloys." Journal of Nuclear Materials 399(2-3): 146-153.

Hill, D. J. (2008). "Nuclear energy for the future." Nature Materials 7(1): 680-682.
Horton, L. L., J. Bentley and K. Farrell (1982). " A TEM Study of neutron-irradiated iron." Journal of Nuclear Materials 108-109: 222-233.
Hussein, A. M. and J. A. El-Awady (2016). "Quantifying dislocation microstructure evolution and cyclic hardening in fatigued face-centered cubic single crystals." Journal of the Mechanics and Physics of Solids 91: 126-144.
Jamond, O., R. Gatti, A. Roos and B. Devincre (2016). "Consistent formulation for the Discrete-Continuous Model: Improving complex dislocation dynamics simulations." International Journal of Plasticity 80: 19-37.
Jiao, Q., J. Cheng, G.-D. Sim, S. Ghosh and J. A. El-Awady (2021). "Micro-mechanical investigation of the thermo-mechanical properties of micro-architectured tungsten coatings." Journal of the Mechanics and Physics of Solids 150: 104326.
Jiao, Z. and G. S. Was (2010). "The role of irradiated microstructure in the localized deformation of austenitic stainless steels." Journal of Nuclear Materials 407(1): 34-43.
Jourdan, T., G. Bencteux and G. Adjanor (2014). "Efficient simulation of kinetics of radiation induced defects: A cluster dynamics approach." Journal of Nuclear Materials 444(1-3): 298-313.
Khiara, N., F. Onimus, S. Jublot-Leclerc, T. Jourdan, T. Pardoen, J.-P. Raskin and Y. Bréchet (2021). "In-situ TEM irradiation creep experiment revealing radiation induced dislocation glide in pure copper." Acta Materialia 216: 117096.
Kirsanov, V. V., S. B. Kislitsin and E. M. Kislitsina (1991). "Atom—atom collision cascades in non-uniformly stressed metals." Philosophical Magazine A 64(1): 201-211.
Kohnert, A. A. and L. Capolungo (2019). "A novel approach to quantifying the kinetics of point defect absorption at dislocations." Journal of the Mechanics and Physics of Solids 122: 98-115.
Kohnert, A. A. and B. D. Wirth (2015). "Cluster dynamics models of irradiation damage accumulation in ferritic iron. I. Trap mediated interstitial cluster diffusion." Journal of Applied Physics 117(15): 154305.
Kohnert, A. A. and B. D. Wirth (2015). "Cluster dynamics models of irradiation damage accumulation in ferritic iron. II. Effects of reaction dimensionality." Journal of Applied Physics 117(15): 154306.
Kohnert, A. A., B. D. Wirth and L. Capolungo (2018). "Modeling microstructural evolution in irradiated materials with cluster dynamics methods: A review." Computational Materials Science 149: 442-459.
Lee, E. H., T. S. Byun, J. D. Hunn, M. H. Yoo, K. Farrell and L. K. Mansur (2001). "On the origin of deformation microstructures in austenitic stainless steel: Part I - Microstructures." Acta Materialia 49: 3269–3276.
Lei, J., H. Ding, G.-g. Shu and Q.-m. Wan (2014). "Study on the mechanical properties evolution of A508-3 steel under proton irradiation." Nuclear Instruments and Methods in Physics Research Section B: Beam Interactions with Materials and Atoms 338: 13-18.
Li, Y., M. Boleininger, C. Robertson, L. Dupuy and S. L. Dudarev (2019). "Diffusion and interaction of prismatic dislocation loops simulated by stochastic discrete dislocation dynamics." Physical Review Materials 3(7): 073805.
Li, Y., G. Po and N. Ghoniem (2020). "Coupled cluster-dislocation dynamics of irradiation-induced defects." Materialia 14: 100891.
Li, Y., C. Robertson, M. Shukeir and L. Dupuy (2018). "Screw dislocation interaction with irradiation defect-loops in α-iron: evaluation of cross-slip effect using dislocation dynamics simulations." Modelling and Simulation in Materials Science and Engineering 26(5): 055009.
Li, Z., Z. Liu, Z. Zhuang and Y. Cui (2021). "Temperature dependent deformation localization in irradiated tungsten." International Journal of Plasticity 146: 103077.

Lin, Y.-R., A. Bhattacharya, D. Chen, J.-J. Kai, J. Henry and S. J. Zinkle (2021). "Temperature-dependent cavity swelling in dual-ion irradiated Fe and Fe-Cr ferritic alloys." Acta Materialia 207: 116660.
Liu, F., A. C. F. Cocks and E. Tarleton (2020). "A new method to model dislocation self-climb dominated by core diffusion." Journal of the Mechanics and Physics of Solids 135: 103783.
Liu, F. X., Z. L. Liu, X. Y. Pei, J. Q. Hu and Z. Zhuang (2017). "Modeling high temperature anneal hardening in Au submicron pillar by developing coupled dislocation glide-climb model." International Journal of Plasticity 99: 102-119.
Liu, X. Y. and S. B. Biner (2008). "Molecular dynamics simulations of the interactions between screw dislocations and self-interstitial clusters in body-centered cubic Fe." Scripta Materialia 59(1): 51-54.
Lu, S., Q. Kan, M. Zaiser, Z. Li, G. Kang and X. Zhang (2022). "Size-dependent yield stress in ultrafine-grained polycrystals: A multiscale discrete dislocation dynamics study." International Journal of Plasticity 149: 103183.
Lugiato, L. A., P. Mandel and L. M. Narducci (1984). "Adiabatic elimination in nonlinear dynamical systems." Physical Review A 29(3): 1438-1452.
Makin, M. J. (1964). "The long-range forces between dislocation loops and dislocations." Philosophical Magazine 10(106): 695-711.
Mamivand, M., P. Wells, H. Ke, S. Shu, G. R. Odette and D. Morgan (2019). "CuMnNiSi precipitate evolution in irradiated reactor pressure vessel steels: Integrated Cluster Dynamics and experiments." Acta Materialia 180: 199-217.
Marian, J. and V. V. Bulatov (2011). "Stochastic cluster dynamics method for simulations of multispecies irradiation damage accumulation." Journal of Nuclear Materials 415(1): 84-95.
Matijasevic, M., E. Lucon and A. Almazouzi (2008). "Behavior of ferritic/martensitic steels after n-irradiation at 200 and 300°C." Journal of Nuclear Materials 377(1): 101-108.
Matijasevic, M., W. Van Renterghem and A. Almazouzi (2009). "Characterization of irradiated single crystals of Fe and Fe–15Cr." Acta Materialia 57(5): 1577-1585.
McMurtrey, M. D., B. Cui, I. Robertson, D. Farkas and G. S. Was (2015). "Mechanism of dislocation channel-induced irradiation assisted stress corrosion crack initiation in austenitic stainless steel." Current Opinion in Solid State and Materials Science 19(5): 305-314.
Mesarovic, S. D. (2017). "Dislocation Creep: Climb and Glide in the Lattice Continuum." Crystals 7(8): 273.
Meslin, E., A. Barbu, L. Boulanger, B. Radiguet, P. Pareige, K. Arakawa and C. C. Fu (2008). "Cluster-dynamics modelling of defects in α-iron under cascade damage conditions." Journal of Nuclear Materials 382(2-3): 190-196.
Nordlund, K., S. J. Zinkle, A. E. Sand, F. Granberg, R. S. Averback, R. E. Stoller, T. Suzudo, L. Malerba, F. Banhart, W. J. Weber, F. Willaime, S. L. Dudarev and D. Simeone (2018). "Primary radiation damage: A review of current understanding and models." Journal of Nuclear Materials 512: 450-479.
Osetsky, Y. N. and D. J. Bacon (2003). "Void and precipitate strengthening in α-iron: what can we learn from atomic-level modelling?" Journal of Nuclear Materials 323(2-3): 268-280.
Osetsky, Y. N. and D. J. Bacon (2005). "Comparison of void strengthening in fcc and bcc metals: Large-scale atomic-level modelling." Materials Science and Engineering: A 400-401: 374-377.
Osetsky, Y. N. and D. J. Bacon (2010). "Atomic-scale mechanisms of void hardening in bcc and fcc metals." Philosophical Magazine 90(7-8): 945-961.
Osetsky, Y. N., D. J. Bacon and V. Mohles (2003). "Atomic modelling of strengthening mechanisms due to voids and copper precipitates in α-iron." Philosophical Magazine 83(31-34): 3623-3641.

Osetsky, Y. N., D. J. Bacon, B. N. Singh and B. Wirth (2002). "Atomistic study of the generation, interaction, accumulation and annihilation of cascade-induced defect clusters." Journal of Nuclear Materials 307–311: 852–861.

Osetsky, Y. N. and D. Rodney (2020). Atomic-Level Dislocation Dynamics in Irradiated Metals. Comprehensive Nuclear Materials: Second Edition. 1: 663–688.

Osetsky, Y. N., R. E. Stoller, D. Rodney and D. J. Bacon (2005). "Atomic-scale details of dislocation–stacking fault tetrahedra interaction." Materials Science and Engineering: A 400-401: 370-373.

Pakarinen, J., S. Tähtinen and B. N. Singh (2013). "A comparative TEM study of in-reactor and post-irradiation tensile tested copper." Journal of Nuclear Materials 442(1-3): S821-S825.

Patra, A. and D. L. McDowell (2015). "A void nucleation and growth based damage framework to model failure initiation ahead of a sharp notch in irradiated bcc materials." Journal of the Mechanics and Physics of Solids 74: 111-135.

Po, G., Y. Cui, D. Rivera, D. Cereceda, T. D. Swinburne, J. Marian and N. Ghoniem (2016). "A phenomenological dislocation mobility law for bcc metals." Acta Materialia 119: 123-135.

Po, G. and N. Ghoniem (2013). "Continuum modeling of plastic flow localization in irradiated fcc metals." Journal of Nuclear Materials 442(1-3): S607-S611.

Po, G., M. Lazar, D. Seif and N. Ghoniem (2014). "Singularity-free dislocation dynamics with strain gradient elasticity." Journal of the Mechanics and Physics of Solids 68: 161-178.

Po, G., M. S. Mohamed, T. Crosby, C. Erel, A. El-Azab and N. Ghoniem (2014). "Recent Progress in Discrete Dislocation Dynamics and Its Applications to Micro Plasticity." Jom 66(10): 2108-2120.

Pokor, C., Y. Brechet, P. Dubuisson, J. P. Massoud and A. Barbu (2004). "Irradiation damage in 304 and 316 stainless steels: experimental investigation and modeling. Part I: Evolution of the microstructure." Journal of Nuclear Materials 326(1): 19-29.

Reali, L., M. R. Wenman, A. P. Sutton and D. S. Balint (2021). "Plasticity of zirconium hydrides: a coupled edge and screw discrete dislocation model." Journal of the Mechanics and Physics of Solids 147: 104219.

Rovelli, I., S. L. Dudarev and A. P. Sutton (2017). "Non-local model for diffusion-mediated dislocation climb and cavity growth." Journal of the Mechanics and Physics of Solids 103: 121-141.

Seeger, A. (1958). 2nd UN Conference on Peaceful Uses of Atomic Energy. United Nations, New York 6, pp. 250.

Shang, Z., C. Fan, J. Ding, S. Xue, A. Gabriel, L. Shao, T. Voisin, Y. M. Wang, T. Niu, J. Li, T. D. De la Rubia, H. Wang and X. Zhang (2021). "Heavy ion irradiation response of an additively manufactured 316LN stainless steel." Journal of Nuclear Materials 546: 152745.

Singh, B. N., D. J. Edwards, S. Tähtinen, P. Moilanen, P. Jacquet and J. Dekeyser (2004). Final report on in-reactor tensile tests on OFHC-copper and CuCrZr alloy. Risø-R-1481(EN).

Singh, B. N., A. Horsewell and P. Toft (1999). "Effects of neutron irradiation on microstructure and mechanical properties of pure iron." Journal of Nuclear Materials 271&272: 97-101.

Singh, B. N., S. Tähtinen, P. Moilanen, P. Jacquet and J. Dekeyser (2003). "In-reactor uniaxial tensile testing of pure copper at a constant strain rate at 90 °C." Journal of Nuclear Materials 320(3): 299-304.

Sobie, C., N. Bertin and L. Capolungo (2015). "Analysis of Obstacle Hardening Models Using Dislocation Dynamics: Application to Irradiation-Induced Defects." Metallurgical and Materials Transactions A 46(8): 3761-3772.

Sobie, C., L. Capolungo, D. L. McDowell and E. Martinez (2017). "Scale transition using dislocation dynamics and the nudged elastic band method." Journal of the Mechanics and Physics of Solids 105: 161-178.

Sobie, C., L. Capolungo, D. L. McDowell and E. Martinez (2017). "Thermal activation of dislocations in large scale obstacle bypass." Journal of the Mechanics and Physics of Solids 105: 150-160.

Soneda, N. and T. D. De La Rubia (2001). "Migration kinetics of the self-interstitial atom and its clusters in bcc Fe." Philosophical Magazine A 81(2): 331-343.

Swenson, M. J. and J. P. Wharry (2015). "The comparison of microstructure and nanocluster evolution in proton and neutron irradiated Fe–9%Cr ODS steel to 3 dpa at 500 °C." Journal of Nuclear Materials 467: 97-112.

Tehranchi, A., X. Zhang, G. Lu and W. A. Curtin (2017). "Hydrogen–vacancy–dislocation interactions inα-Fe." Modelling and Simulation in Materials Science and Engineering 25(2): 025001.

Terentyev, D., D. J. Bacon and Y. N. Osetsky (2008). "Interaction of an edge dislocation with voids in α-iron modelled with different interatomic potentials." Journal of Physics: Condensed Matter 20(44): 445007.

Terentyev, D., P. Grammatikopoulos, D. J. Bacon and Y. N. Osetsky (2008). "Simulation of the interaction between an edge dislocation and a ⟨100⟩ interstitial dislocation loop in α-iron." Acta Materialia 56(18): 5034-5046.

Terentyev, D., G. Monnet and P. Grigorev (2013). "Transfer of molecular dynamics data to dislocation dynamics to assess dislocation–dislocation loop interaction in iron." Scripta Materialia 69(8): 578-581.

Terentyev, D., X. Xiao, A. Dubinko, A. Bakaeva and H. Duan (2015). "Dislocation-mediated strain hardening in tungsten: Thermo-mechanical plasticity theory and experimental validation." Journal of the Mechanics and Physics of Solids 85: 1-15.

Tondro, A. and H. Abdolvand (2021). "Quantifying hydrogen concentration in the vicinity of zirconium hydrides and deformation twins." Journal of the Mechanics and Physics of Solids 148: 104287.

Trinkaus, H., B. N. Singh and S. I. Golubov (2000). "Progress in modelling the microstructural evolution in metals under cascade damage conditions." Journal of Nuclear Materials 283-287: 89-98.

Van Renterghem, W., D. Terentyev and M. J. Konstantinović (2018). "Transmission electron analysis of dislocation loops in T91 steels from MEGAPIE and MIRE irradiation experiments." Journal of Nuclear Materials 506: 43-52.

Victoria, M., N. Baluc, C. Bailat, Y. Dai, M. I. Luppo, R. Schaeublin and B. N. Singh (2000). "The microstructure and associated tensile properties of irradiated fcc and bcc metals." Journal of Nuclear Materials 276: 114-122.

Wang, Y., J. Ding, S. Huang, J. Zhao and Y. Wang (2018). "Mesoscale modeling of irradiation damage evolution in bcc iron and vanadium: A comparative study." Fusion Engineering and Design 137: 303-311.

Was, G. S., D. Farkas and I. M. Robertson (2012). "Micromechanics of dislocation channeling in intergranular stress corrosion crack nucleation." Current Opinion in Solid State and Materials Science 16(3): 134-142.

Woo, C. H. (1984). "Irradiation creep due to elastodiffusion." Journal of Nuclear Materials 120: 54-66.

Xia, Z., J. Zhang, Q. Tong and S. Ding (2019). "Multi-physics modeling of delayed hydride cracking in zirconium alloys." Journal of the Mechanics and Physics of Solids 132: 103677.

Xiao, X. (2019). "Fundamental Mechanisms for Irradiation-Hardening and Embrittlement: A Review." Metals 9(10): 1132.

Xiao, X., D. Terentyev and L. Yu (2019). "Model for the spherical indentation stress-strain relationships of ion-irradiated materials." Journal of the Mechanics and Physics of Solids 132: 103694.

Yu, Q., S. Chatterjee, K. J. Roche, G. Po and J. Marian (2021). "Coupling crystal plasticity and stochastic cluster dynamics models of irradiation damage in tungsten." Modelling and Simulation in Materials Science and Engineering 29: 055021.
Zhu, Y., J. Wang, Y. Xiang and X. Guo (2017). "A three-scale homogenisation approach to the prediction of long-time absorption of radiation induced interstitials by nanovoids at interfaces." Journal of the Mechanics and Physics of Solids 105: 1-20.
Zhu, Y., Y. Xiang and K. Schulz (2016). "The role of dislocation pile-up in flow stress determination and strain hardening." Scripta Materialia 116: 53-56.
Zinkle, S. J. (2020). Radiation-Induced Effects on Microstructure. Comprehensive Nuclear Materials 2nd edition. 1: 91-129.
Zinkle, S. J. and J. T. Busby (2009). "Structural materials for fission & fusion energy." Materials Today 12(11): 12-19.
Zinkle, S. J. and B. N. Singh (2006). "Microstructure of neutron-irradiated iron before and after tensile deformation." Journal of Nuclear Materials 351(1-3): 269-284.
Zinkle, S. J. and G. S. Was (2013). "Materials challenges in nuclear energy." Acta Materialia 61(3): 735-758.